SLAC-PUB-12492
April 2007

Performance of a High Resolution Cavity Beam Position Monitor System

Sean Walston [g,*], Stewart Boogert [d], Carl Chung [g], Pete Fitsos [g], Joe Frisch [i], Jeff Gronberg [g], Hitoshi Hayano [k], Yosuke Honda [k], Yury Kolomensky [b], Alexey Lyapin [h], Stephen Malton [h], Justin May [i], Douglas McCormick [i], Robert Meller [f], David Miller [h], Toyoko Orimoto [b,j], Marc Ross [i,a], Mark Slater [c], Steve Smith [i], Tonee Smith [i], Nobuhiro Terunuma [k], Mark Thomson [c], Junji Urakawa [k], Vladimir Vogel [e], David Ward [c], Glen White [i]

[a] *Fermi National Accelerator Laboratory, Batavia, Illinois, USA*
[b] *University of California and Lawrence Berkeley National Laboratory, Berkeley, California, USA* [1]
[c] *University of Cambridge, Cambridge, UK* [2]
[d] *Royal Holloway, University of London, Egham, UK*
[e] *Deutsches Elektronen-Synchrotron, Hamburg, Germany*
[f] *Cornell University, Ithaca, New York, USA* [3]
[g] *Lawrence Livermore National Laboratory, Livermore, California, USA* [4]
[h] *University College London, London, UK* [2]
[i] *Stanford Linear Accelerator Center, Menlo Park, California, USA* [5]
[j] *California Institute of Technology, Pasadena, California, USA*
[k] *High Energy Accelerator Research Organization (KEK), Tsukuba-shi, Ibaraki-ken, Japan* [6]

Abstract

It has been estimated that an RF cavity Beam Position Monitor (BPM) could provide a position measurement resolution of less than one nanometer. We have developed a high resolution cavity BPM and associated electronics. A triplet comprised of these BPMs was installed in the extraction line of the Accelerator Test Facility (ATF) at the High Energy Accelerator Research Organization (KEK) for testing with its ultra-low emittance beam. The three BPMs were each rigidly mounted inside an alignment frame on six variable-length struts which could be used to move the BPMs in position and angle. We have developed novel methods for extracting the position and tilt information from the BPM signals including a robust calibration algorithm which is immune to beam jitter. To date, we have demonstrated a position resolution of 15.6 nm and a tilt resolution of 2.1 μrad over a dynamic range of approximately ± 20 μm.

Key words: Cavity Beam Position Monitor; BPM; Accelerator Test Facility; ATF; International Linear Collider; ILC

* Corresponding author. Lawrence Livermore National Laboratory, 7000 East Ave., L-305, Livermore, CA 94550. Tel.: 925-423-7364; fax: 925-423-3371.
Email address: walston2@llnl.gov (Sean Walston).

[1] This work was supported in part by the US Department of Energy under Contract DE-FG02-03ER41279.
[2] This work was supported by the Commission of the European Communities under the 6th Framework Programme "Structuring the European Research Area," contract number RIDS-011899.
[3] This work was supported by the National Science Foundation.
[4] This work was performed under the auspices of the U.S. Department of Energy by the University of California, Lawrence Livermore National Laboratory under contract W-7405-Eng-48.

Work supported in part by US Department of Energy contract DE-AC02-76SF00515

1. Introduction

The design for the International Linear Collider (ILC) calls for beams which are focused down to a few nanometers at the interaction point. This poses unique engineering challenges which must be overcome. To wit, final focus components must be effectively stabilized at the nanometer level.

Some years ago, LINX was proposed as a new facility at SLAC to support engineering studies of, among other things, stabilization techniques for beamline components [1]. One goal was to demonstrate nanometer stability of colliding beams. Located in the SLD collider hall, LINX was to reuse much of the existing hardware of the SLC and SLD. During the Nanobeam 2002 Workshop in Lausanne, Switzerland in September of that year, it was suggested that nanometer resolution beam position monitors (BPMs) could verify the nanometer level vibration stability without the LINX beam-beam collision project. The intent of our experiment is to understand the limits of BPM performance and evaluate their applicability to issues posed by the ILC.

The intrinsic resolution of a BPM is limited by the signal to noise ratio of the system: The signal voltage of the BPM is determined by the beam's energy loss to the antisymmetric transverse magnetic TM_{110} mode (discussed in some detail in Section 2.1) and by the external coupling of the waveguide; the overall noise of the system comes from thermal and electronic noise as well as contamination from the symmetric transverse magnetic TM_{010} mode. It has been estimated that an RF cavity BPM along with state-of-the-art waveform processing could have a resolution below one nanometer [2].

With sufficient resolution, other beam-diagnostic measurements are also feasible. For example, a finite-length bunch having either a non-zero angle of obliquity or angle of attack (relative to the orientation of the cavity) produces a signal – hereafter referred to simply as "tilt" – which is in quadrature to the position signal produced by a simple displacement of a very short bunch. It is therefore possible to independently measure both the position and tilt of the beam by using in-phase/quadrature-phase (I/Q) demodulation of the signal from the cavity BPM: The conversion from I and Q to position and tilt is a simple rotation.

[5] This work was supported by the U.S. Department of Energy under contract DE-AC02-76SF00515.

[6] This work was supported by the Japan-USA Collaborative Research Grant, Grant-in-Aid for Scientific Research from the Japan Society for the Promotion of Science.

2. Theory of Cavity BPMs

2.1. *Electromagnetic Fields in a Cavity*

When a bunch transits a cavity, the field of the bunch excites the eigenmodes of the electromagnetic fields within the cavity. For the case of a cavity in the shape of a right circular cylinder (ignoring the effects of the beam pipe openings), the frequencies of the eigenmodes naturally depend on the length L and radius R of the cavity. For cavities with $L < 2.03R$ (the case in the present experiment), the first transverse magnetic (TM) mode is the fundamental oscillation of the cavity [3].

For beams near the center of the cavity, the TM_{010} (monopole) mode has the highest excitation of all the modes, is symmetric, and is proportional to the charge of the bunch. The explicit expressions for the fields of the TM_{010} mode are

$$E_z = CJ_0\left(\frac{j_{01}r}{R}\right)e^{i\omega_{010}t} \tag{1}$$

$$H_r = 0 \tag{2}$$

$$H_\phi = -iC\frac{\omega_{010}\epsilon_0 R}{j_{01}}J_0'\left(\frac{j_{01}r}{R}\right)e^{i\omega_{010}t}. \tag{3}$$

where C is proportional to the amplitude of the oscillation, J_m is a Bessel function of the first kind of order m, and j_{mn} is the nth root of the equation $J_m(j) = 0$; $j_{01} = 2.405$ [4]. In general, the resonant angular frequency ($\omega = 2\pi f$) is

$$\omega_{mnp} = c\sqrt{\left(\frac{j_{mn}}{R}\right)^2 + \left(\frac{p\pi}{L}\right)^2}. \tag{4}$$

The fields for the monopole mode are illustrated in Figure 1.

The TM_{110} or dipole mode, however, is antisymmetric and its amplitude has a strong linear dependence on the transverse offset of the beam relative to the electrical center of the cavity; the power thus has a quadratic dependence on the offset. The phase depends on the direction of the offset. The explicit expressions for the fields of the TM_{110} mode are

$$E_z = CJ_1\left(\frac{j_{11}r}{R}\right)\cos(\phi)e^{i\omega_{110}t} \tag{5}$$

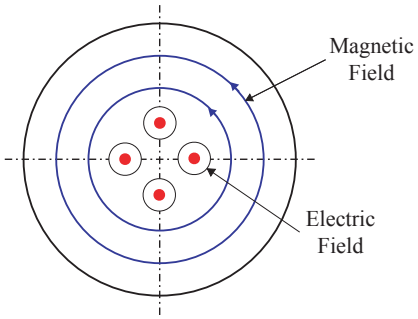

Fig. 1. The fields of the TM_{010} or monopole mode. The amplitude of the monopole mode is proportional to the bunch charge.

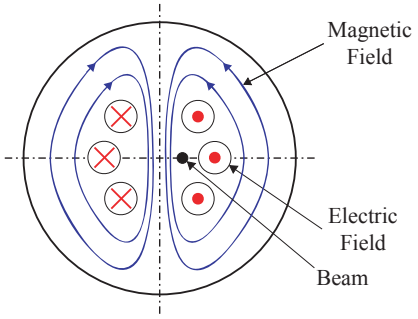

Fig. 2. The fields of the TM_{110} or dipole mode. The amplitude of the dipole mode has a strong dependence on offset of the beam relative to the electrical center of the cavity.

$$H_r = -iC\frac{\omega_{110}\epsilon_0 R^2}{j_{11}^2 r} J_1\left(\frac{j_{11}r}{R}\right)\sin(\phi)e^{i\omega_{110}t} \tag{6}$$

$$H_\phi = -iC\frac{\omega_{110}\epsilon_0 R}{j_{11}} J_1'\left(\frac{j_{11}r}{R}\right)\cos(\phi)e^{i\omega_{110}t} \tag{7}$$

where $j_{11} = 3.832$ [4]. These fields are illustrated in Figure 2.

Physical cavities have finite values for the quality factor $\mathcal{Q}$: They dissipate energy in the cavity walls and also lose energy to the external waveguides and ultimately the readout electronics. Each of the cavity's resonant frequencies is therefore not simply a single frequency but rather is smeared out, and appreciable excitations can occur over a narrow band of frequencies around the eigenfrequency. The monopole mode can therefore have a finite tail at the dipole mode frequency, as illustrated in Figure 3. These components cannot be simply filtered out.

2.2. *Energy in a Cavity*

The exchange of energy between the beam and the cavity depends entirely on the geometry of the

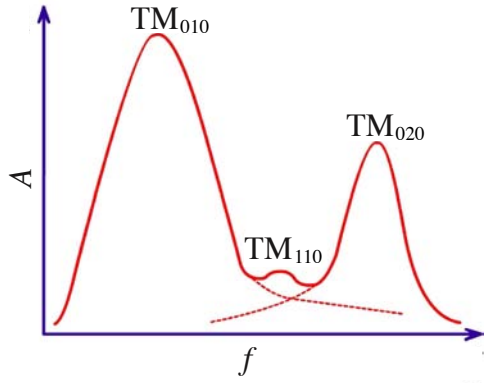

Fig. 3. Amplitude vs. frequency for the first two monopole modes and first dipole mode of a cylindrical cavity. The first two monopole modes surround the (usually) much smaller amplitude dipole mode, and because of the finite $\mathcal{Q}$ of the cavity, have components at the dipole mode frequency.

cavity and the properties of the bunch rather than on the cavity material. It can be characterized by the normalized shunt impedance

$$\frac{\mathcal{R}}{\mathcal{Q}} = \frac{V^2}{\omega W} \tag{8}$$

where ω is the frequency, W is the energy stored in the cavity, and

$$V = \left|\int_{-L/2}^{L/2} E_z dz\right|, \tag{9}$$

all calculated for the mode of interest of the cavity. For the TM_{110} mode, it is convenient to define a shunt impedance $[\mathcal{R}/\mathcal{Q}]_0$ which corresponds to a beam passing through the cavity on a trajectory offset from the electrical center by an amount x_0,

$$\frac{\mathcal{R}}{\mathcal{Q}} = \left[\frac{\mathcal{R}}{\mathcal{Q}}\right]_0 \frac{x^2}{x_0^2}. \tag{10}$$

The energy left in an initially empty cavity after a Gaussian distributed bunch of length σ_z and charge q passes through it can be calculated as [5]

$$W = \frac{\omega}{4}\left[\frac{\mathcal{R}}{\mathcal{Q}}\right]_0 \frac{x^2}{x_0^2} q^2 \exp\left(-\frac{\omega^2\sigma_z^2}{c^2}\right), \tag{11}$$

where c is the speed of the light (assuming the bunch is relativistic).

The external quality factor of the cavity describes the strength of the cavity coupling to the output network, and may be expressed as

$$\mathcal{Q}_{\rm ext} = \frac{\omega W}{P_{\rm out}}. \tag{12}$$

Only a portion of the energy in Eq. (11) proportional to $1/\mathcal{Q}_{\rm ext}$ will be coupled out of the cavity. The power coming from the cavity just after the excitation is thus

$$P_{\rm out} = \frac{\omega^2}{4\mathcal{Q}_{\rm ext}} \left[\frac{\mathcal{R}}{\mathcal{Q}}\right]_0 \frac{x^2}{x_0^2} q^2 \exp\left(-\frac{\omega^2\sigma_z^2}{c^2}\right), \tag{13}$$

assuming the stored energy over one cycle is nearly constant (i.e. the period of oscillation $T = 2\pi/\omega$ is much less than the decay time τ). The voltage in an output line with impedance Z is then

$$V_{\rm out} = \frac{\omega}{2}\sqrt{\frac{Z}{\mathcal{Q}_{\rm ext}}\left[\frac{\mathcal{R}}{\mathcal{Q}}\right]_0} \exp\left(-\frac{\omega^2\sigma_z^2}{2c^2}\right) q\frac{x}{x_0}. \tag{14}$$

Over a range out to approximately two-thirds of the beam pipe radius (depending at some level on the ratio of the beam pipe and cavity diameters, and the overall linearity of the system), the voltage is linearly proportional to the beam offset x. The terms which collectively constitute the coefficient on x thus represent the sensitivity of the BPM and can be used to predict the resolution of the system.

As the energy stored in the cavity decays, the output power also decays. It is important to include here both the power going into the output network as well as the power dissipated in the cavity walls. The latter depends on the wall material and is described by the internal quality factor,

$$\mathcal{Q}_0 = \frac{\omega W}{P_{\rm diss}}. \tag{15}$$

The decay is exponential with a decay constant τ which may be written as

$$\tau = \frac{\mathcal{Q}_L}{\omega} \tag{16}$$

where

$$\frac{1}{\mathcal{Q}_L} = \frac{1}{\mathcal{Q}_0} + \frac{1}{\mathcal{Q}_{\rm ext}}. \tag{17}$$

The total energy coupled out from the cavity can be determined by integrating the output power,

$$W_{\rm out} = \int_0^\infty P_{\rm out} e^{-\frac{t}{\tau}} dt = P_{\rm out}\tau. \tag{18}$$

2.3. *Signals from a Cavity BPM*

For a BPM system employing the $\rm TM_{110}$ mode, a bunch of charge q, length σ_z, and passing through the cavity on a trajectory parallel to but displaced from the z-axis by an amount x thus induces in the output line a voltage

$$V_x(t) = V_{\rm out} e^{-\frac{t}{2\tau}} \sin(\omega t) \tag{19}$$

where $V_{\rm out}$ is defined in Eq. (14). The response of a cavity BPM to more complex beam profiles is discussed in detail elsewhere [6].

Consider a finite length bunch, the centroid of which passes through the cavity along the z-axis, but where the bunch has some angle of attack α. The response of a cavity to such a bunch is most easily understood by imagining the bunch as being comprised of a series of particles, distributed along z, and each having charge dq. Each particle's displacement x as it passes through the cavity is then $z\tan(\alpha)$. If the bunch is Gaussian distributed in z, dq may be defined as

$$dq = \frac{q}{\sqrt{2\pi}\sigma_z} \exp\left(-\frac{z^2}{2\sigma_z^2}\right) dz. \tag{20}$$

The voltage induced in the output line by such a bunch is then

$$\begin{aligned} V_\alpha(t) = {} & \frac{\omega}{2}\sqrt{\frac{Z}{\mathcal{Q}_{\rm ext}}\left[\frac{\mathcal{R}}{\mathcal{Q}}\right]_0} \frac{q}{\sqrt{2\pi}\sigma_z} \frac{\tan(\alpha)}{x_0} \\ & \times \int_{-\infty}^{\infty} \left\{ z \exp\left(-\frac{z^2}{2\sigma_z^2}\right) \exp\left[-\frac{1}{2\tau}\left(t - \frac{z}{c}\right)\right] \right. \\ & \left. \times \sin\left[\omega\left(t - \frac{z}{c}\right)\right] \right\} dz. \end{aligned} \tag{21}$$

Evaluating the integral yields

$$\begin{aligned} V_\alpha(t) = {} & -\frac{\omega}{2}\sqrt{\frac{Z}{\mathcal{Q}_{\rm ext}}\left[\frac{\mathcal{R}}{\mathcal{Q}}\right]_0} \frac{q\sigma_z^2\tan(\alpha)}{x_0} e^{-\frac{t}{2\tau}} \\ & \times \exp\left[\frac{\sigma_z^2}{2}\left(\frac{1}{4\tau^2c^2} - \frac{\omega^2}{c^2}\right)\right] \left\{ \sin(\omega t) \right. \\ & \times \left[\frac{1}{2\tau c}\cos\left(\frac{\sigma_z^2\omega}{2\tau c^2}\right) + \frac{\omega}{c}\sin\left(\frac{\sigma_z^2\omega}{2\tau c^2}\right)\right] \\ & - \cos(\omega t)\left[\frac{1}{2\tau c}\sin\left(\frac{\sigma_z^2\omega}{2\tau c^2}\right)\right. \\ & \left. \left. - \frac{\omega}{c}\cos\left(\frac{\sigma_z^2\omega}{2\tau c^2}\right)\right] \right\}. \end{aligned} \tag{22}$$

Some important limits can be deduced by comparing the decay time τ, the period of oscillation of the cavity $T = 2\pi/\omega$, and the time required for the bunch to transit the cavity σ_z/c. In the limits where $T \ll \tau$ (equivalent to $\omega/c \gg 1/2\tau c$), $\sigma_z/c \ll \tau$, and $\sigma_z/c \lesssim T$, or in any case $\sigma_z^2\omega/2\tau c^2 \ll 1$, Eq. (22) reduces to

$$V_\alpha(t) \cong -\frac{\omega}{2}\sqrt{\frac{Z}{\mathcal{Q}_{\text{ext}}}\left[\frac{\mathcal{R}}{\mathcal{Q}}\right]_0}\frac{q\omega\sigma_z^2\tan(\alpha)}{x_0 c} \times \exp\left(-\frac{\omega^2\sigma_z^2}{2c^2}\right)e^{-\frac{t}{2\tau}}\cos(\omega t). \quad (23)$$

Consider a beam through the center of the cavity, but on a trajectory with some angle of obliquity θ relative to the z-axis. The response of a cavity to such a beam is most easily understood by imagining the physical cavity as being comprised of many thin cavities stacked along z. The beam passes straight through each with a displacement $x = z\tan(\theta)$. Defining the length of each cavity as dz, the signal dV from each is proportional to dz/L. The total signal may thus be summed by integration:

$$V_\theta(t) = \frac{\omega}{2}\sqrt{\frac{Z}{\mathcal{Q}_{\text{ext}}}\left[\frac{\mathcal{R}}{\mathcal{Q}}\right]_0}\exp\left(-\frac{\omega^2\sigma_z^2}{2c^2}\right)\frac{q\tan(\theta)}{x_0} \times\frac{1}{L}\int_{-L/2}^{L/2}\left(z\exp\left\{-\frac{1}{2\tau}\left[t+\frac{z}{c\cos(\theta)}\right]\right\} \times\sin\left\{\omega\left[t+\frac{z}{c\cos(\theta)}\right]\right\}\right)dz. \quad (24)$$

Defining

$$a = \frac{1}{2\tau c\cos(\theta)}, \quad (25)$$

$$b = \frac{\omega}{c\cos(\theta)}, \quad (26)$$

and evaluating the integral yields

$$V_\theta(t) = \frac{\omega}{2}\sqrt{\frac{Z}{\mathcal{Q}_{\text{ext}}}\left[\frac{\mathcal{R}}{\mathcal{Q}}\right]_0}\exp\left(-\frac{\omega^2\sigma_z^2}{2c^2}\right)\frac{q\tan(\theta)}{Lx_0} \times e^{-\frac{t}{2\tau}}\left(\sin(\omega t)\left\{\cosh\left(\frac{aL}{2}\right)\frac{a}{a^2+b^2} \times\left[L\cos\left(\frac{bL}{2}\right)-\frac{4b}{a^2+b^2}\sin\left(\frac{bL}{2}\right)\right] +\sinh\left(\frac{aL}{2}\right)\frac{1}{a^2+b^2}\left[bL\sin\left(\frac{bL}{2}\right) -2\frac{a^2-b^2}{a^2+b^2}\cos\left(\frac{bL}{2}\right)\right]\right\}+\cos(\omega t) \times\left\{\sinh\left(\frac{aL}{2}\right)\frac{a}{a^2+b^2}\left[L\sin\left(\frac{bL}{2}\right) +\frac{4b}{a^2+b^2}\cos\left(\frac{bL}{2}\right)\right] -\cosh\left(\frac{aL}{2}\right)\frac{1}{a^2+b^2}\left[bL\cos\left(\frac{bL}{2}\right) +2\frac{a^2-b^2}{a^2+b^2}\sin\left(\frac{bL}{2}\right)\right]\right\}\right). \quad (27)$$

The limit where $T \ll \tau$ (equivalently $a \ll b$), and the limit where the transit time for the bunch to cross the cavity $L/c\cos(\theta) \ll \tau$ (equivalently $aL/2 \ll 1$), Eq. (27) reduces to

$$V_\theta(t) \cong \frac{\omega}{2}\sqrt{\frac{Z}{\mathcal{Q}_{\text{ext}}}\left[\frac{\mathcal{R}}{\mathcal{Q}}\right]_0}\exp\left(-\frac{\omega^2\sigma_z^2}{2c^2}\right)\frac{q\tan(\theta)}{Lx_0} \times e^{-\frac{t}{2\tau}}\cos(\omega t)\left\{\frac{2c^2\cos^2(\theta)}{\omega^2}\sin\left[\frac{\omega L}{2c\cos(\theta)}\right] -\frac{Lc\cos(\theta)}{\omega}\cos\left[\frac{\omega L}{2c\cos(\theta)}\right]\right\}. \quad (28)$$

In the limit of a short cavity where $L/c\cos(\theta) \ll T$ (or equivalently $bL/2 \ll 1$), $V_\theta(t) \propto L^2$. However, the limit $L/c\cos(\theta) \ll T$ is not always reliable, and in such cases, $V(t)$ deviates noticeably from a simple L^2 dependence.

It should also be noted that the voltage induced in the output line by a bunch passing through the cavity on a trajectory parallel to but displaced from the z-axis by an amount x is $\pi/2$ out of phase from that induced by either a bunch of length σ_z passing axially through the center of the cavity with an angle of attack α, or a beam passing through the center on a trajectory with an angle of obliquity θ:

$$V_x \propto xe^{-\frac{t}{2\tau}}\sin(\omega t), \quad (29)$$

$$V_\alpha \propto -\alpha e^{-\frac{t}{2\tau}}\cos(\omega t), \quad (30)$$

$$V_\theta \propto \theta e^{-\frac{t}{2\tau}}\cos(\omega t) \quad (31)$$

(in the limits of $\alpha \ll 1$ and $\theta \ll 1$).

The theory of cavity BPMs is discussed in more detail elsewhere [5, 6].

3. Experimental Setup

This experiment employed three identical cavity BPMs designed at the Budker Institute of Nuclear Physics (BINP) [7]. A quarter view of the material

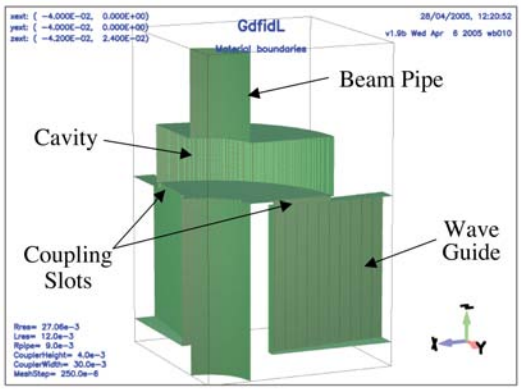

Fig. 4. A quarter view of the inside surface of a BINP BPM.

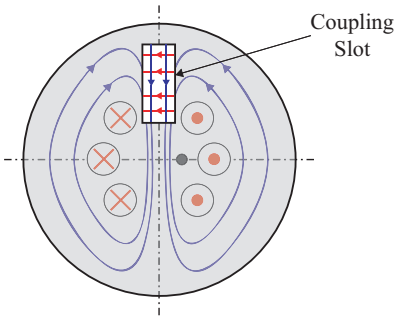

Fig. 5. The dipole mode was selectively coupled out by means of two long, narrow, radial slots on one face of the cavity. The electric field vector points circumferentially across the slot while the magnetic field vector points radially. (The slot shown is not to scale and is for illustrative purposes.) The cavities had two orthogonal slots corresponding to x and y.

boundaries of the BINP BPM cavities is shown in Figure 4.

The dipole mode — whose amplitude is comparatively small when the beam passes near the electrical center of the cavity — was selectively coupled out by two orthogonal slots: These slots — one each for x and y — exploited the difference in the field structure of the monopole and dipole modes to reject the tails of the monopole mode with frequencies at or near the dipole mode frequency. This is illustrated in Figure 5.

The nominal dimensions of the cavities are detailed in Table 1. The machining tolerances were nominally between 10 μm and 20 μm for turning (e.g. the cavity and beam pipe surfaces) and approximately 25 μm for milling (e.g. the coupling slots) [8]. In the process of mounting the three BPMs in the alignment frame however, detailed measurements of the beam pipe of each BPM were made using a coordinate measuring machine (CMM). The results of these measurements are listed in Table 2 and

Length of cavity	12.00 mm
Radius of cavity	27.06 mm
Radius of beam pipe	10.00 mm
Coupling slot dimensions	1.50 mm × 12.00 mm

Table 1
BINP BPM nominal cavity dimensions.

BPM Number	Measurement Location	Diameter (mm)	Roundness (μm)
1	Upstream	20.0418	43.9
	Center	20.0880	45.6
	Downstream	20.0505	49.9
2	Upstream	20.0411	240.0
	Center	20.0341	196.8
	Downstream	19.9694	195.3
3	Upstream	19.9750	108.5
	Center	20.0519	96.0
	Downstream	20.0794	84.1

Table 2
Diameter and roundness [9] measurements of the beam pipes for the three BINP BPMs. Each beam pipe was measured in three locations along z: An upstream location near the upstream vacuum flange ($z = 0$); a center location near the cavity at $z = +35$ mm; and a downstream location near the downstream vacuum flange at $z = +80$ mm. Each measurement was performed on a Zeiss CMM using a 290 point scan.

strongly suggest that the nominal tolerances were perhaps not achieved. The more critical measurements with the CMM of the cavity surfaces and coupling slots would require cutting the cavities open and have therefore not been performed as of this writing.

The nominal resonant frequency of the dipole TM_{110} mode was 6426 MHz. Before final installation of the cavities in the alignment frame, the x and y ports of each cavity were connected to a network analyzer, and by squeezing the cavities in a particular way with a C-clamp, the x and y modes were made to be very nearly degenerate. This process resulted in TM_{110} mode frequencies which were increased slightly to approximately 6429 MHz.

To these three BPMs must be added a fourth "reference" cavity whose signal was used to normalize the amplitudes from the three position cavities to remove the effects of variations in the bunch charge. This signal also provided a single reference for comparing the phases of the signals from the three position cavities. The signal from the reference cavity

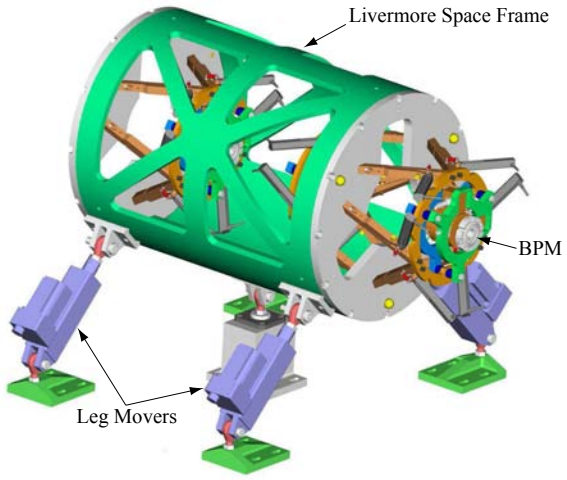

Fig. 6. The space frame served as the mounting platform for the three BPMs.

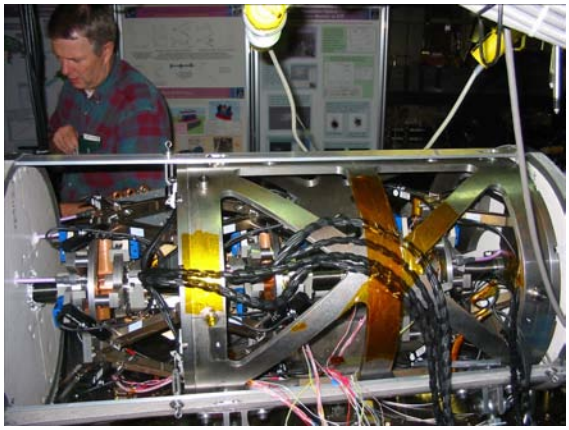

Fig. 7. The NanoBPM experiment in situ on the extraction line of the ATF.

was split with one part being passed through a crystal detector to determine the beam's arrival time. The nominal resonant frequency of the monopole TM_{010} mode was 6426 MHz. This frequency was subsequently raised to 6429 MHz so as to match the three BPMs (if the reference cavity has the same resonant frequency, phase errors resulting from an error in the determination of the beam's arrival time cancel out of Eqs. 32 and 33).

The three BPMs were rigidly mounted inside an alignment frame consisting of a cylindrical steel space frame which was designed and built at the Lawrence Livermore National Lab (LLNL). The first vibrational mode of the space frame was at a frequency of 200 Hz. The entire space frame assembly was mounted by four variable-length motorized legs and a non-motorized variable-length center strut which allowed the alignment frame to be moved in x, y, yaw, pitch, and roll. The physical layout of the experiment is illustrated in Figure 6. The NanoBPM experiment, in situ on the extraction line at ATF, is shown in Figure 7.

Each BPM was rigidly mounted to the endplates of the space frame by six variable-length struts, illustrated in Figure 8, which allowed it to be moved by small amounts in x, y, z, yaw, pitch, and roll. The hexapod arrangement of the struts was inherently stiff, and coupled with the rigidity of the space frame allowed only rigid-body motion of the three BPMs to a high degree. A strut is pictured in Figure 9.

Single bunch extractions from the ATF ring were used for all of our tests. Each ATF extraction contained between 6 and 7×10^9 e^- at an energy of 1.28

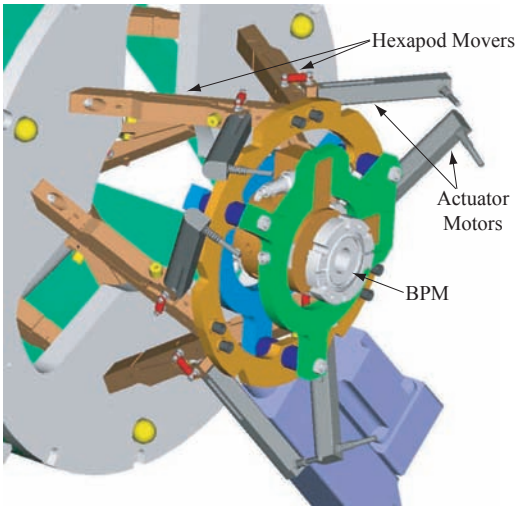

Fig. 8. The BPMs were mounted on hexapod strut movers.

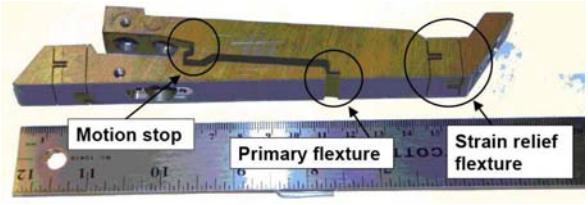

Fig. 9. Each hexapod strut employed a flexure with approximately a 12 to 1 mechanical advantage, i.e. a change in the gap results in a 1/12 change in length of the strut.

GeV. The machine repetition rate was ~ 1 Hz.

The electronics used to process the raw signals from the BPMs was designed and built at the Stanford Linear Accelerator Center (SLAC). It may be summarized as follows:

(i) Bandpass filter centered at 6426 MHz with 225 MHz bandwidth: Removed out-of-band signals and most notably monopole mode which, due to imperfect coupling slots, may not have been completely rejected.
(ii) Amplifier, 20 dB gain.
(iii) Mixer, 5950 MHz LO: Mix down to 476 MHz.
(iv) Lowpass filter, 700 MHz cutoff: Removed residual LO signal.
(v) Amplifier, 20 dB gain.
(vi) Bandpass filter centered at 476 MHz with 20 MHz bandwidth: Removed out-of-band noise which could be aliased into the signal band.
(vii) Mixer, 456 MHz LO: Mix down to 26 MHz.
(viii) Lowpass filter, 30 MHz cutoff: Removed residual LO signal.
(ix) Amplifier, 16 dB gain.
(x) Lowpass filter, 30 MHz cutoff: Removed out-of-band noise which could be aliased into the signal band.
(xi) Digitizer, 14 bit, 100 megasamples per second.

A schematic diagram is shown in Figure 10.

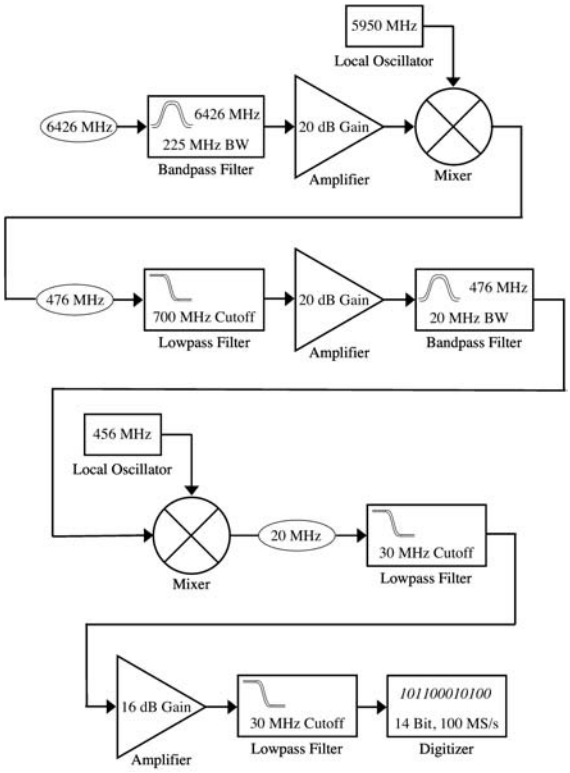

Fig. 10. The electronics used to process the signals from each channel.

4. Waveform Processing

In order to tease out the beam's position and trajectory from the skein of raw BPM signals, precise determinations of the amplitudes and phases of the digitized waveforms were needed. In time, the waveforms were nominally exponentially decaying sine waves. Two independent methods, fitting and digital down-conversion (DDC), were employed in the determination of the amplitudes A and phases φ. Both are discussed in some detail below. In both, only the unsaturated portions of the waveforms were used.

For each channel i (six in all corresponding to x and y for the three BPMs), the quantities I_i and Q_i corresponding to the real and imaginary parts of the waveform were then calculated by normalizing each amplitude A_i and phase φ_i to the reference cavity amplitude A_{Ref} and phase φ_{Ref},

$$I_i = \frac{A_i}{A_{\mathrm{Ref}}} \cos(\varphi_i - \varphi_{\mathrm{Ref}}) \tag{32}$$

$$Q_i = \frac{A_i}{A_{\mathrm{Ref}}} \sin(\varphi_i - \varphi_{\mathrm{Ref}}). \tag{33}$$

The position and tilt signals, P_i and T_i respectively, were then a rotation in the complex plane from I_i and Q_i,

$$\begin{pmatrix} P_i \\ T_i \end{pmatrix} = \begin{pmatrix} \cos\Theta_i & \sin\Theta_i \\ -\sin\Theta_i & \cos\Theta_i \end{pmatrix} \begin{pmatrix} I_i \\ Q_i \end{pmatrix}, \tag{34}$$

where Θ_i was the IQ-phase for channel i. The quantities x, x', y, and y' (collectively x_i and x'_i) were then proportional to the quantities P and T:

$$x_i = s_i P_i, \tag{35}$$

$$x'_i = s'_i T_i, \tag{36}$$

where s_i and s'_i were the position and tilt scale factors respectively.

The IQ-phases Θ_i, the position scale factors s_i, and the tilt scale factors s'_i were determined from the calibration procedure (described in section 5).

4.1. *Fitting*

The raw waveform $V(t)$ from a given channel was fitted using the equation

$$V(t) = V_0 + Ae^{-\Gamma(t-t_0)} \sin\left[\omega(t-t_0)+\varphi\right], \qquad (37)$$

considering the amplitude A and phase φ as free parameters, and where V_0 was the ADC pedestal value, ω and Γ were the frequency and decay constant of the channel in question, and t_0 was the time when the bunch passed through the apparatus. Only the non-saturated portion of the waveform was used in the fit.

The time when the bunch transited the apparatus, t_0, was determined by fitting for the midpoint of the rise of the signal from the crystal detector. The ADC pedestal value was determined by taking the mean of the ADC samples from before the pulse transited the apparatus.

When fitting for amplitude A and phase φ, ω and Γ were always held fixed. The values of ω and Γ for a given channel were determined as follows: Calibration data was fitted to Equation 37, considering ω and Γ as free parameters in the fit in addition to A and φ. The medians of these fitted values over the calibration set were then taken as the ω and Γ for the channel in question.

4.2. *Digital Down-Conversion*

In the digital down-conversion (DDC) algorithm, the raw waveform from a given channel was multiplied by a complex local oscillator (LO) of the same frequency ω. Low-pass filtering reduced this signal to baseband. The low-pass filter was implemented by convoluting the complex signal with a 39 coefficient, symmetric, finite impulse response (FIR), low-pass filter with 2.5 MHz bandwidth. The demodulated waveform could be written

$$D(t) = \left\{\left[V(t) - V_0\right] e^{i\omega t}\right\} * F \qquad (38)$$

where $V(t)$ was the raw waveform from the ADC, V_0 was the ADC pedestal value as determined by taking the mean of the ADC samples from before the pulse transited the apparatus, ω was the frequency of the channel in question, and F was the filter vector. A series of demodulated waveforms are illustrated in Figure 11.

The complex amplitudes for a set of data were defined by evaluating $D(t)$ at a fixed time t_1 chosen to optimize the ratio of signal to noise. If at t_1 a demodulated waveform was corrupted by saturation, the complex amplitude was evaluated early in the non-saturated portion of the demodulated waveform and extrapolated back to t_1 using the decay constant Γ and frequency ω.

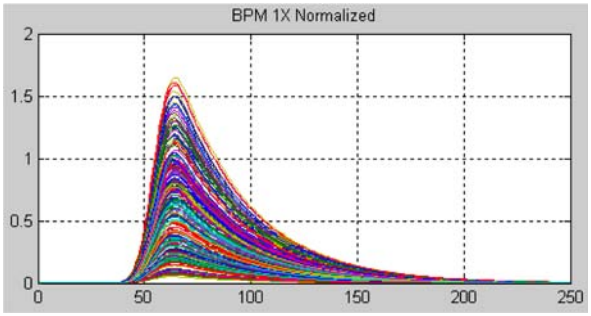

Fig. 11. Demodulated waveforms from BPM 1, x for a data set. Each line represents a separate ATF extraction and has been normalized by the corresponding amplitude of the reference cavity. In the plot, the x axis refers to the sample number where the sample period was 10 ns.

5. Calibration

The calibration procedure described here determined the IQ-phase Θ_i, and the position and tilt scale factors s_i and s_i' respectively for both the x and y channels of each of the three BPMs in a manner which eliminated the effects of beam jitter and drift.

5.1. *IQ-Phase Determination*

For a given transverse direction, x or y, the value of I or Q in any one BPM should be related by a linear equation to the values of I and Q in the other two BPMs since the 1.28 GeV beam travels through the three BPMs in a very nearly straight line:

$$I_i = a + \sum_{j\neq i} \left(b_j I_j + c_j Q_j\right), \qquad (39)$$

$$Q_i = d + \sum_{j\neq i} \left(f_j I_j + g_j Q_j\right), \qquad (40)$$

where $i, j = 1, 2, 3$. We desired to find the values of the coefficients a, b and c, and d, f and g which would allow us to predict I and Q in one BPM from the values of I and Q in the other two. Repeated application of Eqs. (39) and (40) for many ATF extractions yielded a set of simultaneous equations which could be expressed in terms of a single matrix equation $\mathbf{b} = \mathbf{A}\mathbf{x}$, where $\mathbf{x}$ was a column vector comprised of the coefficients a, b and c, or d, f and g, $\mathbf{b}$ was a column vector of the measured values for either I or Q from a given BPM, and $\mathbf{A}$ was the matrix of Is and Qs from the other two BPMs. The matrix $\mathbf{A}$ also contained a column of 1s which allowed for the constant terms a or d. Each row of $\mathbf{A}$ and $\mathbf{b}$ corresponded to a single ATF extraction. Once $\mathbf{A}$ and $\mathbf{b}$

were known, the question became how to find the optimal solution to the equation for the coefficients a, b, and c or d, f, and g in $\mathbf{x}$. We chose the method of singular value decomposition (SVD) to invert the non-square and possibly singular $m \times n$ matrix $\mathbf{A}$ to yield the matrix $\mathbf{A}^+$: This method has the property that the solution $\mathbf{x} = \mathbf{A}^+\mathbf{b}$ minimizes the magnitude $|\mathbf{Ax} - \mathbf{b}|$ [10].

Once these coefficients were known, events where BPM i had been moved were then considered, and ΔI_i and ΔQ_i were defined as the difference between the predicted and measured values for I_i and Q_i respectively: Then

$$\Delta I_i = I_i - \left[a + \sum_{j \neq i} (b_j I_j + c_j Q_j) \right], \tag{41}$$

$$\Delta Q_i = Q_i - \left[d + \sum_{j \neq i} (f_j I_j + g_j Q_j) \right], \tag{42}$$

$(i, j = 1, 2, 3)$ and any significant deviation from zero of ΔI_i and ΔQ_i was attributed to the change in position of BPM i. For pure translations of BPM i, the values of ΔI_i and ΔQ_i lay along a straight line defining the position axis. ΔQ_i could then be regressed against ΔI_i,

$$\Delta Q_i = A_i \Delta I_i + B_i, \tag{43}$$

and repeated application of Eqs. (41), (42), and (43) for many ATF extractions yielded sets of simultaneous equations which could each be evaluated using SVD. The IQ-phase Θ_i was the arctangent of A_i.

5.2. *Position Scale Factors*

The determination of the position scale factors s_i began by noting that the trajectory of the beam between BPMs 1 and 2 was the same as that between 2 and 3, irrespective of how the BPMs had been moved. The electrical centers of BPMs 1 and 3, in their nominal positions, were used to define a coordinate axis, and BPM 2 was allowed to have an offset with respect to that axis. This is shown schematically in Fig. 12, and may be written mathematically as

$$\frac{(m_2 + x_2 + s_2 P_2) - (m_1 + s_1 P_1)}{z_{12}} = \frac{(m_3 + s_3 P_3) - (m_2 + x_2 + s_2 P_2)}{z_{23}}, \tag{44}$$

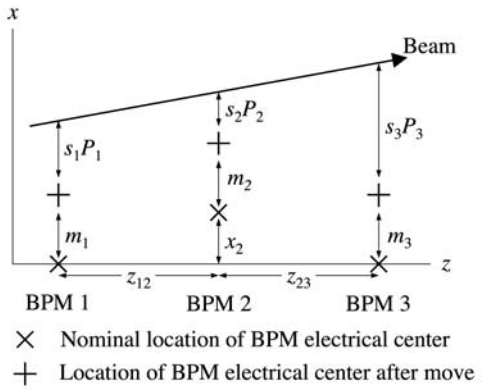

Fig. 12. The nominal positions of the electrical centers of BPMs 1 and 3 define the coordinate system, and BPM 2 is allowed to have a relative offset: These are denoted above with a $\times$. Each BPMs is then moved in turn away from its nominal position by a known amount m_n. The new position for the electrical center of the BPM is denoted by a $+$. The quantity z_{mn} is the distance between BPMs along the beamline.

where m_n denotes the amount BPM n has been moved away from its nominal position by the hexapod struts, and where x_2 denotes the offset of BPM 2 relative to the axis defined by the electrical centers of BPMs 1 and 3. The BPMs were moved one at a time resulting in four linearly independent configurations. Repeated application of Eq. (44) over multiple bunch crossings covering the four linearly independent configurations again yielded a set of simultaneous equations which could be evaluated using SVD to solve for the four unknowns consisting of the offset x_2 and the three position scale factors s_n.

5.3. *Tilt Scale Factors*

In one respect, the tilt signals were more difficult to calibrate because it was impossible to separate the contribution to the tilt signal due to the angle of obliquity of the beam from that due to the angle of attack of the bunch (both relative to the orientation of the cavity). However, the trajectory of the beam could be independently determined from its positions registered in the other two BPMs, and this in turn could be related to the angle of obliquity by a constant θ_i which was the nominal orientation of the cavity relative to the electrical centers of the other two BPMs. The average angle of attack over a series of ATF extractions was assumed to be nearly constant, or in any case fluctuations were assumed to be small compared to the other terms, most notably the tilt t_i of the BPM as applied by the hexa-

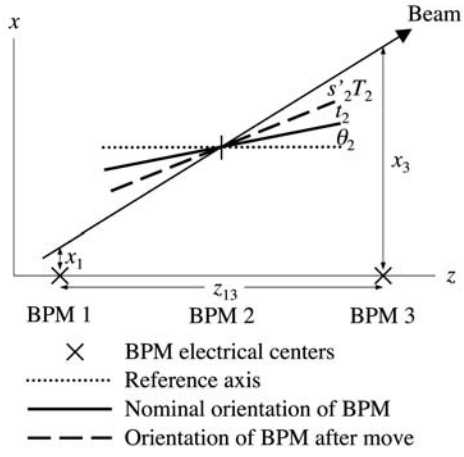

Fig. 13. When calibrating the tilt scale factors s'_i for a given BPM, the electrical centers of the other two BPMs defined the coordinate system. The beam's trajectory was determined relative to this coordinate system by the position signals in those two BPMs. The nominal orientation of the BPM in question relative to this coordinate system θ_i, the applied tilt t_i, and the scaled tilt signal s'_iT_i, added together, should equal the beam trajectory, as illustrated.

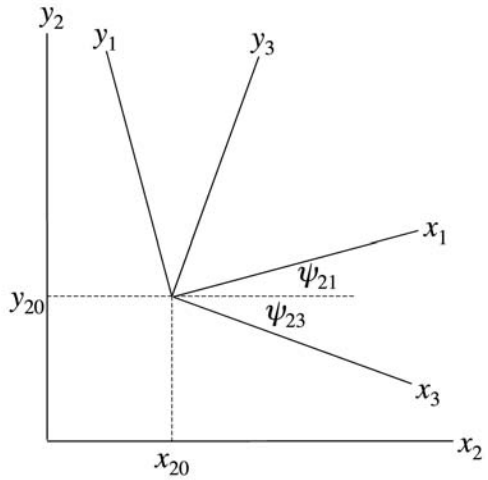

Fig. 14. Let the axis defined by the electrical centers of BPMs 1 and 3 be the origin in the xy planes of all three BPMs: The coordinates associated with BPM 2 are then translated by an offset (x_{20}, y_{20}). Further, let the orientation of the x and y axes of BPM 2 define the principle axes of the coordinate system: The orientations of BPMs 1 and 3 will then be rotated relative to BPM 2 by angles ψ_{21} and ψ_{23}, respectively.

pod struts. For a given BPM, the trajectory of the beam as determined from the position signals in the other two BPMs was taken as equal to the sum of θ_i, the angle of applied tilt of the BPM t_i, and the scaled tilt signal s'_iT_i (neglecting the bunch's angle of attack). This is illustrated schematically in Figure 13, and may be written mathematically as

$$\frac{x_k - x_j}{z_{jk}} = s'_iT_i + \theta_i + t_i \tag{45}$$

where $i, j, k = 1, 2, 3$ and $i \neq j \neq k$. For a given BPM, the nominal orientation and the orientation in which a known tilt t_i was applied constituted two linearly independent configurations. Repeated application of Eq. (45) over multiple ATF extractions covering the two configurations again yielded a set of simultaneous equations which could be evaluated using SVD to solve for the two unknowns consisting of the angle of attack offset θ_i and the tilt scale s'_i.

6. BPM Resolution

6.1. *Calibrated BPMs*

BPM resolution was determined by measuring the residual – that is the difference between the position of the beam as measured by the BPM in question and the predicted position as calculated from the beam's position in the two other BPMs. The resolution was then proportional to the standard deviation of the distribution of the residuals over many ATF extractions.

In the right coordinate system, as detailed in Figure 14, the y position of the beam in a given BPM can be related in a straight-forward way to the x and y positions of the beam in the other two BPMs by

$$y_i = y_{i0} + (-1)^i \sum_{j,k=1}^{3} \epsilon_{ijk} \frac{z_i - z_k}{|z_j - z_k|} \times [-\sin(\psi_{ij})x_j + \cos(\psi_{ij})y_j] \tag{46}$$

where y_{i0} is the y offset of BPM i from the axis defined by the electrical centers of BPMs j and k, ϵ_{ijk} is the antisymmetric unit tensor, z_i are the positions along the beam line of the BPMs, and ψ_{ij} is the angle of rotation about the z axis of BPM j relative to BPM i. To the degree that the coupling slots for x and y were not orthogonal, x_i might be correlated with y_i. It was therefore important to exclude x_i from the regression for y_i in Eq. (46) because its inclusion might have artificially reduced the measured resolution. For the specific case of BPM 2, Eq. (46) can be more simply expressed as

$$y_2 = a + b_1x_1 + b_3x_3 + c_1y_1 + c_3y_3. \tag{47}$$

Additional terms could of course be added to Eq. (47) to take into account other effects, and in practice, $x'_{1,3}$ and $y'_{1,3}$ were included. For the example of BPM 2, Eq. (47) thus became

$$y_2 = a + b_1 x_1 + b_3 x_3 + c_1 y_1 + c_3 y_3 + d_1 x'_1 + d_3 x'_3 + f_1 y'_1 + f_3 y'_3 \quad (48)$$

and repeated application of Eq. (48) over many ATF extractions yielded a matrix equation which could be evaluated using the method of SVD to determine the coefficients a, b, c, d, and f.

Once these coefficients had been determined, the residual was calculated as

$$\delta y_2 = y_i - (a + b_1 x_1 + b_3 x_3 + c_1 y_1 + c_3 y_3 + d_1 x'_1 + d_3 x'_3 + f_1 y'_1 + f_3 y'_3)\,. \quad (49)$$

The resolution R was then computed by dividing the standard deviation σ_i of the δy_i distribution by a geometric weight factor. Taking into account only the y-position terms (other terms were small by comparison),

$$R_i = \frac{\sigma_i}{\sqrt{1^2 + \left(\frac{z_{ij} R_j}{z_{jk} R_i}\right)^2 + \left(\frac{z_{ik} R_k}{z_{jk} R_i}\right)^2}}. \quad (50)$$

Because the ATF damping ring involves bends and kickers which operate in the xz plane, the transverse stability of the beam was significantly better in the y direction than in the x direction. The electronics used to process the BPM signals were thus attenuated in channels corresponding to the x direction to avoid saturation by the large signals that were possible. The longest lever arm for constraining the beam's trajectory was that between BPMs 1 and 3. These two facts conspired to make BPM 2, y the channel of choice for measuring the resolution. All three of the BINP BPMs were identical to within tight machining tolerances and $R_i = R_j = R_k$ was assumed. For the specific case of the resolution calculated from the distribution of residuals for BPM 2, y, with $z_{12} = z_{23} = 30$ cm and $z_{13} = 60$ cm,

$$R_{2y} = \frac{\sigma_{2y}}{\sqrt{\left(\frac{1}{2}\right)^2 + 1^2 + \left(\frac{1}{2}\right)^2}}. \quad (51)$$

The tilt resolution R^{Tilt} could be calculated in a similar fashion by relating y' in a given BPM to x, y, x', and y' in the other two BPMs. For the case of BPM 2,

$$y'_2 = a' + b'_1 x_1 + b'_3 x_3 + c'_1 y_1 + c'_3 y_3 + d'_1 x'_1 + d'_3 x'_3 + f'_1 y'_1 + f'_3 y'_3. \quad (52)$$

and coefficients a', b', c', d', and f' were determined in the usual manner by using the method of SVD. The tilt residual $\delta y'_2$ was then defined as

$$\delta y'_2 = y'_i - (a' + b'_1 x_1 + b'_3 x_3 + c'_1 y_1 + c'_3 y_3 + d'_1 x'_1 + d'_3 x'_3 + f'_1 y'_1 + f'_3 y'_3)\,. \quad (53)$$

If the tilt signal were due to the bunch's angle of attack, the geometrical weight factor for BPM 2 would be as in Eq. (51). If, however, the tilt signal were due to the beam's angle of obliquity, the geometric weight factor would simply be unity. Because the tilt signal was comprised of both the bunch's angle of attack and the beam's angle of obliquity, the geometrical weight factor was taken as unity for the tilt resolution R^{Tilt} as a conservative estimate,

$$R^{\mathrm{Tilt}}_{2y} = \sigma^{\mathrm{Tilt}}_{2y}. \quad (54)$$

6.2. *Uncalibrated BPMs*

If the BPMs were uncalibrated, and the beam's position and tilt were not desired, the resolution could nonetheless be computed using an alternate method which evolved from the procedure used to compute the IQ-phase. This alternate method computed the resolution directly from the normalized real and imaginary amplitudes of the waveforms — the I's and Q's — from all the BPM channels, and required moving only a single BPM (usually BPM 2, y) by a known amount.

Considering only ATF extractions where none of the BPMs had been moved away from their nominal positions, the values of I and Q for the channel in question were related by a linear equation to the values of I and Q of the other channels:

$$I_{iy} = p + \sum_{j \neq i} \sum_{a=x,y} (q_{ja} I_{ja} + r_{ja} Q_{ja})\,, \quad (55)$$

$$Q_{iy} = u + \sum_{j \neq i} \sum_{a=x,y} (v_{ja} I_{ja} + w_{ja} Q_{ja})\,. \quad (56)$$

The coefficients p, q, and r and u, v, and w were determined by the method of SVD as usual.

Once these coefficients were known, ATF extractions where BPM i had been moved in the y direction were then considered, and ΔI_{iy} and ΔQ_{iy} were

defined as the difference between the predicted and measured values for I_{iy} and Q_{iy} respectively:

$$\Delta I_{iy} = I_{iy} - \left[p + \sum_{j \neq i} \sum_{a=x,y} \left(q_{ja} I_{ja} + r_{ja} Q_{ja} \right) \right], \quad (57)$$

$$\Delta Q_{iy} = Q_{iy} - \left[u + \sum_{j \neq i} \sum_{a=x,y} \left(v_{ja} I_{ja} + w_{ja} Q_{ja} \right) \right]. \quad (58)$$

Any significant deviation from zero of ΔI_{iy} and ΔQ_{iy} was then attributed to the change in position of BPM i. ΔQ_{iy} could then be regressed against ΔI_{iy} to determine the IQ-phase Θ_i, as in Eq. (43).

The position scale could be calculated from the amount by which BPM i was moved. The distance from the origin to the point defined by the coordinates $(\Delta I_{iy}, \Delta Q_{iy})$ was related to the distance m_{iy} by which the BPM was translated as follows:

$$m_{iy}^2 = y_0^2 + s_i^2 \left(\Delta I_{iy}^2 + \Delta Q_{iy}^2 \right). \quad (59)$$

The constant y_0 (usually close to zero) and the position scale factor s_i were determined by the method of SVD.

The tilt scale factor could be calculated using ATF extractions where the pitch of BPM i had been changed by an amount t_{iy}, as follows:

$$t_{iy} = t_{i0} + s_i' \left(-\Delta I_{iy} \sin \Theta_i + \Delta Q_{iy} \cos \Theta_i \right). \quad (60)$$

The constant t_{i0} (usually close to zero) and the tilt scale factor s_i' were again determined by the method of SVD.

Considering only ATF extractions where none of the BPMs had been moved away from their nominal positions, the residual was then computed as

$$\delta y_i = s_i \left(\Delta I_{iy} \cos \Theta_i + \Delta Q_{iy} \sin \Theta_i \right). \quad (61)$$

The resolution R_i was then determined from the standard deviation of the residual distribution, as in Eq. (51).

The tilt residual was computed as

$$\delta y_i' = s_i' \left(-\Delta I_{iy} \sin \Theta_i + \Delta Q_{iy} \cos \Theta_i \right). \quad (62)$$

The tilt resolution R_i^{Tilt} was then taken as the standard deviation of the tilt residual distribution, as in Eq. (54).

Mode	TM_{010}	TM_{110}
Resonant frequency f (MHz)	4400	6400
Shunt impedance (Ω)	106	0.1 (at 0.5 mm)
Internal quality factor $\mathcal{Q}_0$	6640	6950
External quality factor $\mathcal{Q}_{\mathrm{ext}}$	∞	65000
Loaded quality factor $\mathcal{Q}_L$	6640	6280
Decay time τ (ns)	240	156
Normalized power out P_{norm} ($\sigma_z = 8$ mm) ($\mathrm{W/nC^2/mm^2}$)	—	2.4×10^6
Normalized energy W_{norm} ($\sigma_z = 8$ mm) ($\mathrm{J/nC^2/mm^2}$)	—	0.36

Table 3
Simulated parameters of the BINP BPMs.

7. BPM Output Signals, Noise, and Resolution

In order to estimate the resolution expected from the BPMs, the cavities were simulated using the electromagnetic field simulation code GdfidL [11]. Basic cavity parameters like resonant frequencies and shunt impedances needed for the calculation of the output power were estimated from the simulation. The results are listed in Table 3.

As a means of checking the theoretical assumptions in the simulation, the total energy, normalized by the beam offset and the bunch charge, was calculated from the data on a pulse by pulse basis. The cavities were calibrated such that a bunch with charge q, displaced by an amount x from the electrical center of the cavity, corresponded to a known voltage V_x at the output of the down-conversion electronics. A cut was applied to eliminate saturated waveforms. The normalized total energy was then given by

$$W_{\mathrm{norm}} = \sum_{i=1}^{N} \left(\frac{V_{xi}}{xq} \right)^2 \frac{\Delta t}{GZ}, \quad (63)$$

where the sum was taken over the waveform sam-

Channel	Simulation, Mfr. Spec., or Theory	$1x$	$1y$	$2x$	$2y$	$3x$	$3y$
Resonant frequency f_{110} (MHz)	6400	6429.603 ±0.002	6429.475 ±0.111	6428.759 ±0.002	6429.014 ±0.028	6429.714 ±0.003	6429.380 ±0.007
Normalized energy W_{norm} ($\mathrm{J/nC^2/mm^2}$)	0.36	0.28 ±0.02	0.27 ±0.10	0.36 ±0.02	0.62 ±0.05	0.37 ±0.02	0.44 ±0.04
Decay time τ (ns)	156	167.1 ±0.6	133.1 ±25.3	163.7 ±0.5	153.5 ±13.7	153.1 ±0.9	140.1 ±2.2
Peak power P_{out} for 10^{10} e^- at 1 nm (dBm)	-112.3	-113.6 ±0.2	-112.9 ±2.7	-112.5 ±0.2	-109.8 ±0.9	-112.1 ±0.2	-110.9 ±0.4
Sensitivity for 10^{10} e^- (μV/nm)	0.54	0.47 ±0.01	0.51 ±0.15	0.53 ±0.01	0.72 ±0.07	0.56 ±0.02	0.63 ±0.03
Gain (dB)	39.0	43.7 ±0.1	44.1 ±0.1	43.9 ±0.1	43.4 ±0.1	44.0 ±0.1	45.8 ±0.2
Signal for 10^{10} e^- (ADC Counts/nm)	0.39	0.59 ±0.02	0.67 ±0.23	0.68 ±0.02	0.87 ±0.09	0.73 ±0.02	1.01 ±0.05
Thermal noise power P_{Thermal} ($T = 293$ K and $B = 20$ MHz) (dBm)	-100.9	—					
Noise figure (dB)	3.1	—					
Noise (ADC Counts)	2.1	4.1 ±1.3	4.2 ±1.3	4.4 ±1.4	4.0 ±1.2	4.3 ±1.3	4.2 ±1.3
Expected resolution for 10^{10} e^- (nm)	5.3	6.9 ±2.3	6.4 ±3.2	6.5 ±2.1	4.6 ±1.5	5.9 ±1.8	4.2 ±1.3
Signal bandwidth (MHz)	1.02	1.60 ±0.02	1.59 ±0.2	1.21 ±0.09	1.49 ±0.16	1.59 ±0.05	1.54 ±0.19
Expected noise after DDC (ADC Counts)	0.7	1.4 ±0.5	1.5 ±0.4	1.6 ±0.5	1.4 ±0.4	1.5 ±0.5	1.5 ±0.5
Expected resolution after DDC for 10^{10} e^- (nm)	1.9	2.5 ±0.8	2.2 ±1.1	2.3 ±0.7	1.6 ±0.5	2.1 ±0.7	1.5 ±0.5

Table 4
Comparison of simulated and measured parameters of the BINP BPMs and the expected resolutions calculated therefrom. Absent from these estimates and comparisons are the 20 dB of attenuation present in the x channels.

ples, Δt was the sample time of the waveform, G was the gain of the electronics, and Z was the coaxial line impedance. In our case, $N = 250$, $\Delta t = 10$ ns, and $Z = 50\ \Omega$. The calculation of the normalized energy, $W_{\rm norm}$, included only that portion of the signal due to the position of the beam in the cavity, and excluded the portion of the signal arising from any tilt that the beam may have had. The position signal was proportional to the amplitude of the rotated in-phase component of the waveform. As the magnitude of the signal remained constant under this rotation, the voltage due to the beam position alone, V_x, was related to the total signal by

$$V_x = \frac{I\,\cos\Theta + Q\,\sin\Theta}{\sqrt{(I^2+Q^2)}}\,V_{\rm RMS}. \tag{64}$$

The charge q of each bunch was determined by the amplitude of the monopole mode signal in the reference cavity. The reference cavity in turn was calibrated from the ATF bunch charge data. Histograms of the normalized energy, $W_{\rm norm}$, are shown in Figure 15.

The uncertainty in $W_{\rm norm}$ for each channel was taken as the standard deviation of the distribution over many ATF extractions. Given the close machining tolerances of the cavities, physical differences alone could not account for the variations seen in the estimates for $W_{\rm norm}$ among the six channels. In addition, the ATF current monitor data was not synchronized with the BPM data, and the average amplitude over each 100 pulses had to be used. This contributed an additional uncertainty of perhaps 10-20% in the estimates for $W_{\rm norm}$ for each channel. The uncertainties in the estimates for $W_{\rm norm}$ were likely therefore low. However, the purpose of these estimates of $W_{\rm norm}$ was merely to give some additional credence to the simulation results, and were in no way used to determine the actual resolution of the BPMs.

The decay time for each channel was calculated from the fitted value of Γ (described in Section 4.1),

$$\tau = \frac{1}{2\Gamma}. \tag{65}$$

The uncertainty was determined from the standard deviation of the fitted values of Γ. The theoretical decay time was calculated from Eq. (16).

The peak power coming out of the cavity, $P_{\rm out}$, was then calculated assuming a bunch containing $10^{10}\ e^-$ at a displacement of 1 nm from the electrical center of the cavity.

From this, the intrinsic sensitivity was computed, assuming a coaxial line impedance of 50 Ω.

The theoretical gain of the signal processing electronics was computed from the specifications of the individual components. For comparison, the gain in each channel was measured by feeding a local oscillator signal into the electronics in place of the BPM output. The frequency was adjusted to match that of the cavity so as to pass correctly through the signal processing electronics. The amplitude of the digitized signal was then measured to determine the gain given a power input of −36.3 dBm. These results are shown in Table 4. The uncertainty was taken as the standard deviation over all waveforms from a given channel.

The digital signal could then be estimated from $P_{\rm out}$ using the gain and the characteristics of the digitizer. These results are shown in Table 4 under "Signal".

The thermal noise power of a system is given by

$$P_{\rm Thermal} = kTB \tag{66}$$

where k is Boltzmann's constant, T is the operating temperature, and B is the noise bandwidth. Assuming an operating temperature of 293 K and a bandwidth of 20 MHz (defined by the tightest filter in the electronics), the thermal noise power at the BPM output was found to be −100.9 dBm.

The signal processing electronics both amplified and contributed to the thermal noise inherent in the output of the BPMs. This noise could be seen in the recorded waveforms as random voltage variations around the pedestal value, as shown in Figure 16. The power spectrum of this noise, shown in Figure 17, was found to be flat with an increase over a 20 MHz bandwidth around the final mixdown frequency corresponding to the tightest bandpass filter present in the signal processing electronics. The additional noise introduced into the system by the electronics could be predicted using the specifications of the particular components and applying Friis's formula for noise in a cascaded system [12]:

$$F = F_1 + \frac{F_2 - 1}{G_1} + \frac{F_3 - 1}{G_1\ G_2} + ... \tag{67}$$

where F was the total noise factor of the circuit, F_N was the noise factor of component N and G_N was the gain of component N (all dimensionless ratios). Using Friis's formula, the noise figure was computed to be 3.1 dB.

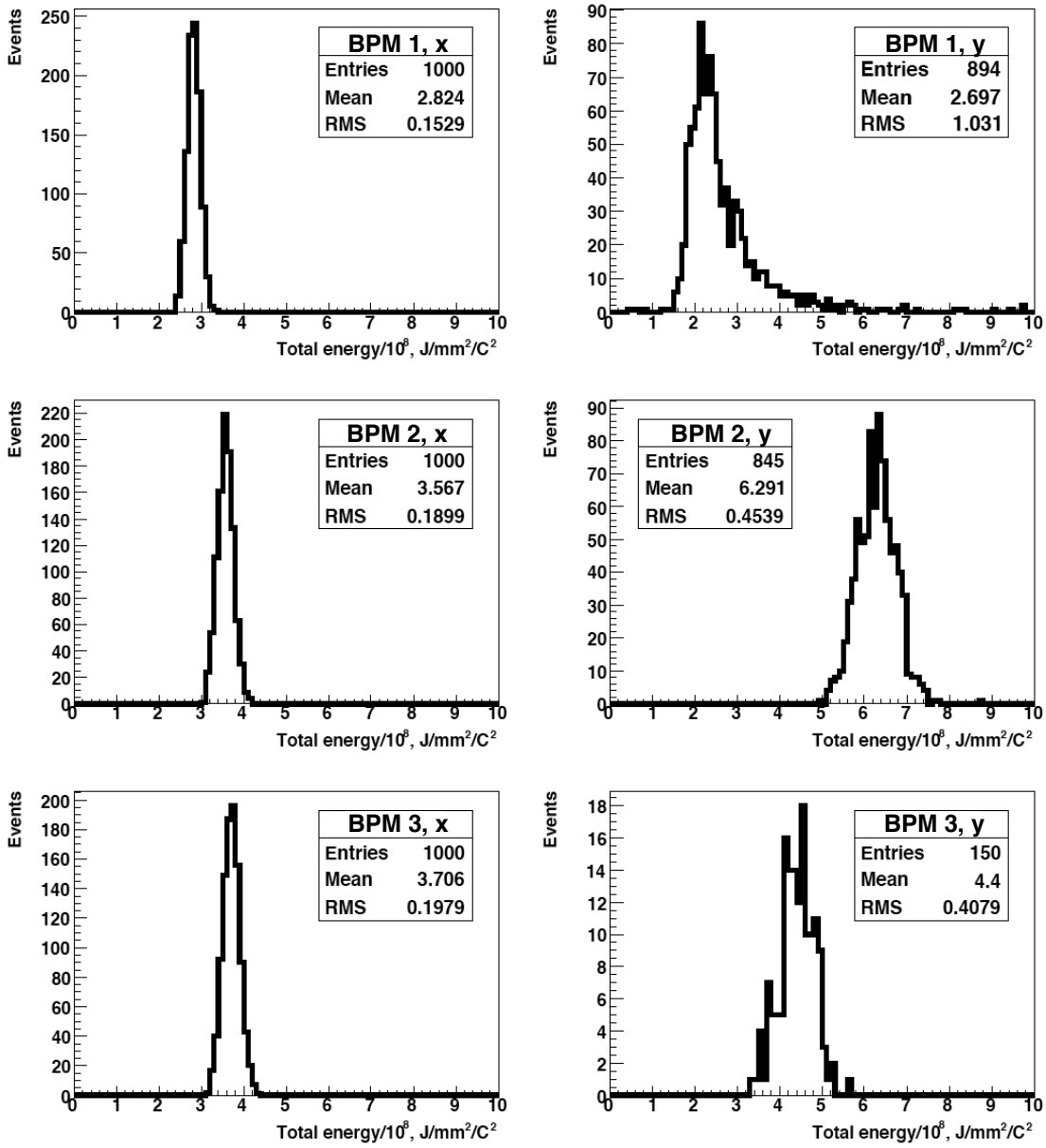

Fig. 15. Histograms of the normalized energy, W_{norm}, for each channel.

The theoretical response of the digitizer to the thermal noise was then calculated as the sum of the thermal noise (-100.9 dBm), the theoretical gain (39.0 dB), and the noise figure from Friis's formula (3.1 dB). These results are summarized in Table 4.

For comparison, the noise in each channel was measured on a pulse by pulse basis by considering the first 20 samples of each waveform corresponding to the time prior to the bunch transiting the apparatus. The pedestal value for each waveform was found by taking the mean of the 20 sample values, and the voltage noise (in ADC counts) was taken as the standard deviation. The noise and associated uncertainty reported in Table 4 is the mean and standard deviation of the measured noise over many ATF extractions.

The inverse of the signal to noise ratio is the resolution of the BPM [2]. The expected resolution after the down-conversion electronics is listed in Table 4.

The bandwidth of the cavity is defined as

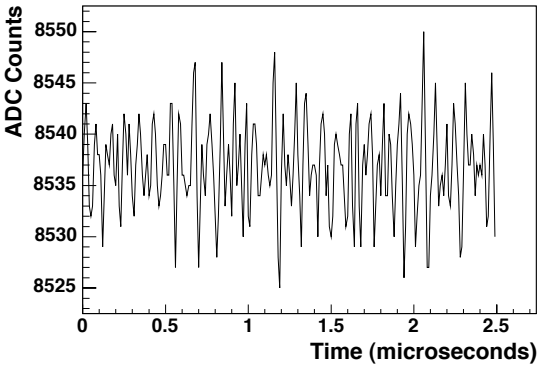

Fig. 16. Noise at the digitizer without any signal.

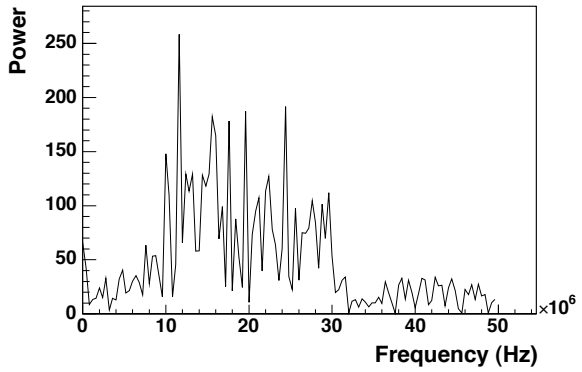

Fig. 17. Noise spectrum found from the Fast Fourier Transform of the noise in Figure 16.

$$B = \frac{f}{\mathcal{Q}_L}, \tag{68}$$

where f is the resonant frequency of the TM_{110} mode, and where $\mathcal{Q}_L$ is defined in Equation 17. For comparison, the signal bandwidth for each channel was estimated by Fast Fourier Transform of the corresponding waveforms in the data. These are shown in Table 4.

The DDC algorithm employed a filter with a 2.5 MHz bandwidth — much tighter that the 20 MHz bandwidth of the signal processing electronics. The thermal noise would thus be reduced by a factor of $\sqrt{2.5\ \mathrm{MHz}/20\ \mathrm{MHz}}$. Because the bandwidths of the signals were sufficiently less than the 2.5 MHz bandwidth of the filter employed by the DDC, the signals were not thought to be appreciably reduced by the DDC algorithm. However, the reduction in noise from the DDC algorithm did produce a corresponding improvement in the expected resolution, as noted in Table 4.

Based on simulations of the cavities and the specifications of the components in the signal processing electronics, the present experiment may thus be expected to produce a position resolution on the order of 1.8 nm.

8. Measured Resolution

8.1. *Measurements*

We present here the results from four data sets, the first taken on the evening of 11 March, 2005, the second taken during the day on 27 May, 2005, and the third and fourth taken early on the morning of 12 April, 2006.

ATF extractions with missing bunches were eliminated from each data set by requiring the reference cavity amplitude to be above a (nearly arbitary but in any case greater than zero) minimum threshold (see Table 5). Each data set was then analyzed using both the fitting and DDC algorithms. The analysis with the fitting algorithm was implemented in ROOT [13], and the fitting was done using MINUIT [14]. Both position and tilt signals (x_1, y_1, x_3, y_3, x_1', y_1', x_3', and y_3') were used in the regression as in Eqs. (48) and (49), described in Section 6.1. The analysis with the DDC algorithm was implemented in MATLAB [15] and the Is and Qs were used directly as in Eqs. (55) through (58), described in Section 6.2. In both cases, nine regression coefficients were determined by the method of SVD.

The data was analyzed by determining the regression coefficients, residuals, and resolution from a single regression utilizing the data set in its entirety. In order not to be at the mercy of a few pathological ATF extractions, a second analysis determined the regression coefficients, residuals, and resolution for groups of (nominally) 100 bunch crossings each.

The data were then reanalyzed after applying loose quality cuts which were choosen to eliminate the small number of poorly reconstructed bunch crossings. This meant requiring the amplitude in all channels to be below a threshold chosen to ensure that the beam was well contained within the dynamic range of all three BPMs. In the case of the fitting algorithm, an additional cut was applied to the fit quality of each waveform. These cuts are detailed in Table 5.

For 2006, a number of minor changes were implemented to try to improve the resolution of the experiment:

Algorithm	Fitting	DDC
Reference Amplitude	$A_{\mathrm{Ref}}(t_0) > 1000$	$\lvert A_{\mathrm{Ref}}(t_1)\rvert > 10$
Amplitude ($i = 1, ..., 6$)	$A_i(t_0) < 25000$	$\lvert A_i(t_1)\rvert < 6000$
Fit Quality	$\chi^2/NDF < 2000$	—

Table 5
Summary of cuts. Amplitudes are in ADC counts and refer to the time specified — t_0 for the fitting algorithm (see section 4.1), and t_1 for the DDC algorithm (see section 4.2). The cut on the reference amplitude A_{Ref} eliminated missing pulses and was always applied. The other cuts were applied when noted (see Table 6).

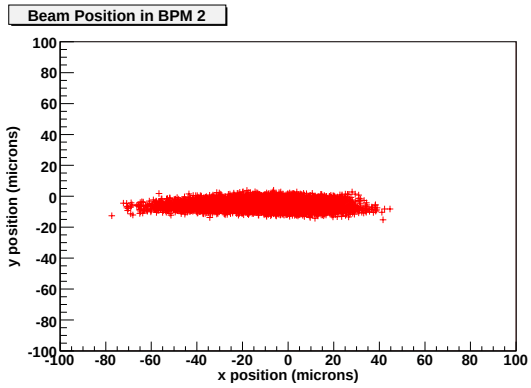

Fig. 18. Beam position as recorded by BPM 2 for 7443 ATF extractions from 11 March 2005, 18:38 JST. The fitting algorithm was employed to compute the beam's position in x and y. The quality cuts were applied.

– Attenuation between the reference cavity and its electronics was reduced to increase its amplitude and improve the signal to noise ratio.
– The BPMs were better centered on the beam in all directions so as to maximize use of dynamic range.
– In February 2006, an improved thermal enclosure was built around the entire experiment to better shield it from temperature changes in the ATF tunnel.

A plot illustrating the characteristic x and y beam stability at the ATF is shown in Fig. 18. Note that the beam stability was much better in y than in x; this resulted from the bends and kickers of the ATF damping ring operating in the xz plane.

Table 6 summarizes the resolutions obtained from these four data sets. The correlation between the measured and predicted beam positions is shown

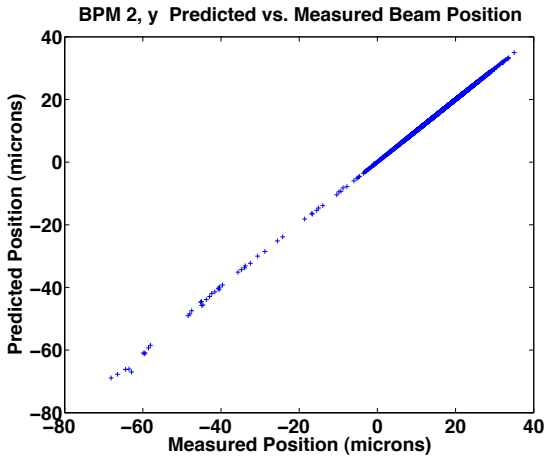

Fig. 19. Predicted beam position vs. measured beam position for 9899 ATF extractions from 27 May 2005, 12:15 JST. The analysis employed the DDC algorithm without quality cuts, and the predicted beam positions were calculated from coefficients determined in one regression using the entire data set. The standard deviation of the distribution was 76.3 nm and the resolution was 62.3 nm. Note that the correlation deteriorated for beam pulses at the extremes, thus illustrating the need for the quality cuts.

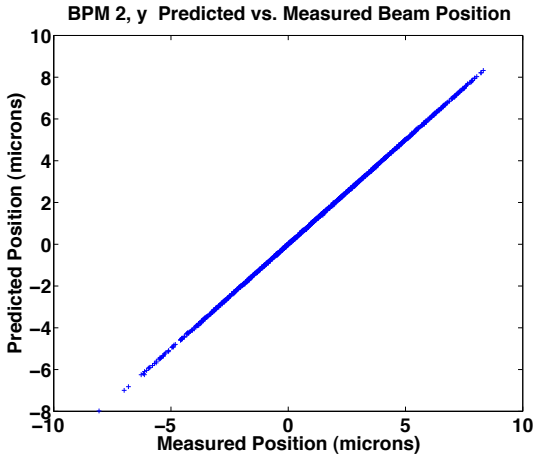

Fig. 20. Predicted beam position vs. measured beam position for 1407 ATF extractions from 12 April 2006, 2:30 JST. The analysis employed the DDC algorithm with quality cuts, and the predicted beam positions were calculated from coefficients determined in one regression using the entire data set. The standard deviation of the distribution was 22.8 nm and the resolution was 18.6 nm.

in Figs. 19 and 20. Typical distributions for the residuals are shown in Figs. 21 and 22. Plotting the residual vs. time indicated that the resolution was

Run Period	Total Bunch Crossings	Algorithm	Cuts	Regressions	Bunch Crossings each Regression	Position Resolution (nm)	Tilt Resolution (μrad)
11 March 2005, 18:38 JST	7500	Fit	No	1	7494	25.2	2.6
		DDC	No	1	7494	42.6	12.6
		Fit	Yes	1	7443	23.8	2.5
		DDC	Yes	1	7481	37.5	3.7
		Fit	No	75	≈ 100	21.8 ± 1.8	1.8 ± 0.2
		DDC	No	75	≈ 100	33.3 ± 2.9	3.6 ± 2.0
		Fit	Yes	75	≈ 100	21.8 ± 1.8	1.8 ± 0.2
		DDC	Yes	75	≈ 100	33.3 ± 2.9	3.3 ± 0.7
27 May 2005, 12:15 JST	9900	Fit	No	1	9899	50.8	—
		DDC	No	1	9899	62.3	—
		Fit	Yes	1	9860	25.4	—
		DDC	Yes	1	9879	25.6	—
		Fit	No	99	≈ 100	25.1 ± 11.0	—
		DDC	No	99	≈ 100	25.7 ± 10.9	—
		Fit	Yes	99	≈ 100	22.9 ± 2.9	—
		DDC	Yes	99	≈ 100	22.4 ± 2.4	—
12 April 2006, 2:16 JST	1100	Fit	No	1	1100	17.6	2.1
		DDC	No	1	1100	16.0	3.9
		Fit	Yes	1	1088	17.6	2.1
		DDC	Yes	1	1066	15.6	2.6
		Fit	No	11	≈ 100	15.7 ± 1.2	1.4 ± 0.2
		DDC	No	11	≈ 100	13.7 ± 1.0	4.1 ± 1.1
		Fit	Yes	11	≈ 100	15.6 ± 1.2	1.4 ± 0.2
		DDC	Yes	11	≈ 100	13.4 ± 1.0	3.2 ± 0.4
12 April 2006, 2:30 JST	1500	Fit	No	1	1496	20.4	2.2
		DDC	No	1	1496	26.1	5.8
		Fit	Yes	1	1454	19.8	2.1
		DDC	Yes	1	1407	18.6	3.3
		Fit	No	15	≈ 100	17.1 ± 1.6	1.5 ± 0.3
		DDC	No	15	≈ 100	17.4 ± 5.6	5.7 ± 2.6
		Fit	Yes	15	≈ 100	16.6 ± 1.2	1.4 ± 0.2
		DDC	Yes	15	≈ 100	14.4 ± 1.3	3.6 ± 0.6

Table 6
Measured resolution from four run periods using both the fitting and DDC algorithms. The data were analyzed with and without quality cuts applied. The coefficients used to calculate the residuals were determined by regressing over the entire data set and by regressing over sets of (nominally) 100 bunch crossings.

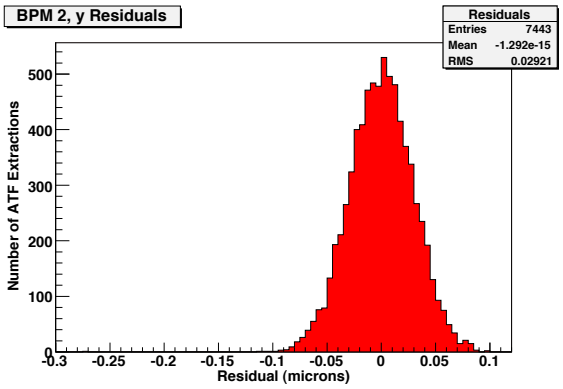

Fig. 21. Residuals for 7443 ATF extractions from 11 March 2005, 18:38 JST. The analysis employed the fitting algorithm with quality cuts and the residuals were calculated from coefficients determined in one regression using the entire data set. The standard deviation of the distribution was 29.2 nm and the resolution was 23.8 nm.

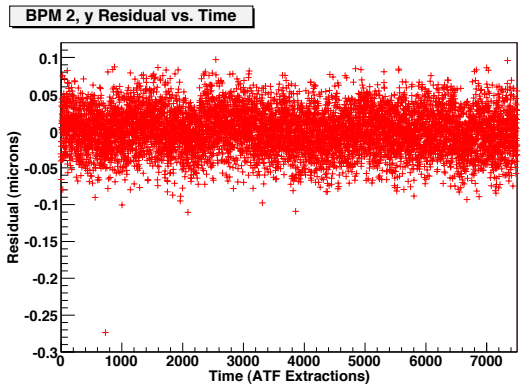

Fig. 23. Residual vs. time for 7443 ATF extractions from 11 March 2005, 18:38 JST. The analysis employed the fitting algorithm with quality cuts and the residuals were calculated from coefficients determined in one regression using the entire data set. The standard deviation of the distribution was 29.2 nm and the resolution was 23.8 nm. The lack of structure suggests the resolution was stable over the period the data was taken.

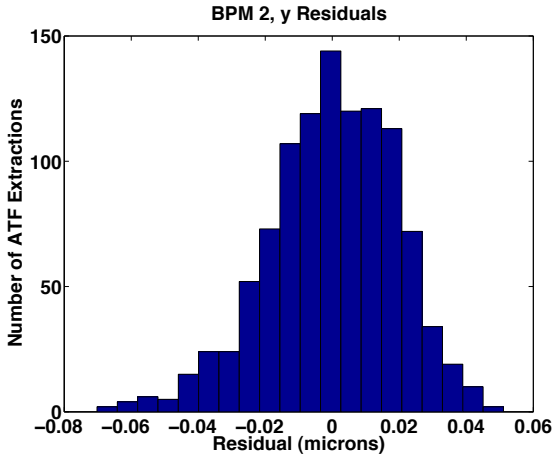

Fig. 22. Residuals for 1066 ATF extractions from 12 Apr, 2006, 2:16 JST. The analysis employed the DDC algorithm with quality cuts and the residuals were calculated from coefficients determined in one regression using the entire data set. The standard deviation of the distribution was 19.1 nm and the resolution was 15.6 nm.

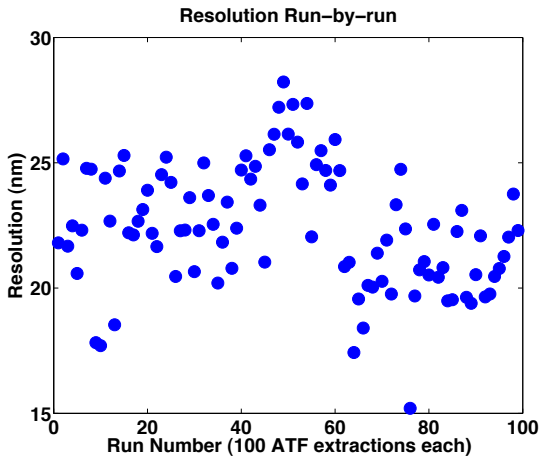

Fig. 24. Resolution for groups of (nominally) 100 sequential bunch crossings from 27 May 2005, 12:15 JST. The analysis employed the DDC algorithm with quality cuts. The mean resolution was 22.4 ± 2.4 nm.

fairly stable over the period the data was taken, as shown in Fig. 23. The same conclusion attained by plotting the resolution from groups of (nominally) 100 sequential ATF extractions vs. time, as shown in Figs. 24 and 25.

The tilt resolution was analyzed analogously to the position resolution. These results are also summarized in Table 6. A typical correlation plot between the measured and predicted beam tilt is shown in Fig. 26. Typical distributions for the tilt residuals are shown in Figs. 27 and 28. The tilt residual also showed stability over the period the data was taken, as plotting the tilt residual vs. time indicates. A characteristic example is shown in Fig. 29. This

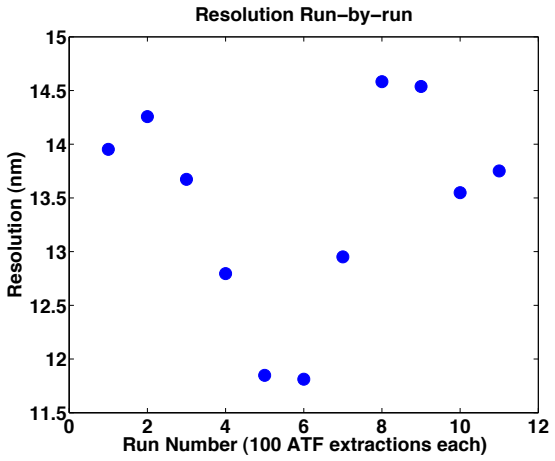

Fig. 25. Resolution for groups of (nominally) 100 sequential bunch crossings from 12 April 2006, 2:16 JST. The analysis employed the DDC algorithm with quality cuts. The mean resolution was 13.4 ± 1.0 nm.

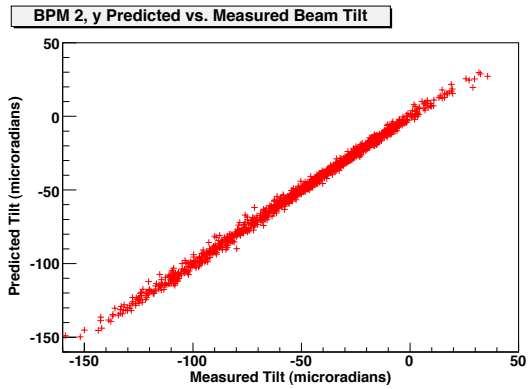

Fig. 26. Predicted beam tilt vs. measured beam tilt for 1454 ATF extractions from 12 April 2006, 2:30 JST. The analysis employed the fitting algorithm with quality cuts, and the predicted beam tilts were calculated from coefficients determined in one regression using the entire data set. The standard deviation of the distribution and the angular resolution was 2.1 μrad.

stability is also suggested by plotting the tilt resolution from groups of (nominally) 100 sequential ATF extractions vs. time, as shown in Figure 30.

8.2. *Other Effects*

Fluctuations in either the local magnetic field or the beam's energy could change the sagitta of the

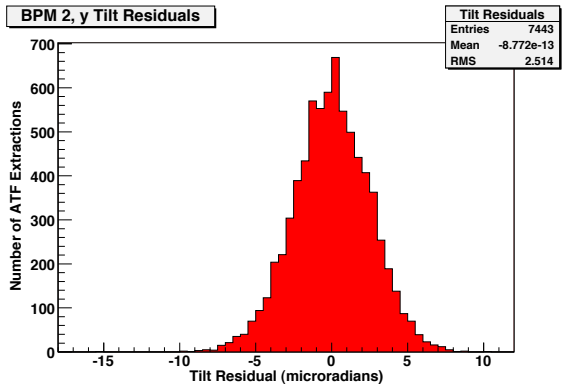

Fig. 27. Tilt residuals for 7443 ATF extractions from 11 March 2005, 18:38 JST. The analysis employed the fitting algorithm with quality cuts and the residuals were calculated from coefficients determined in one regression using the entire data set. The standard deviation of the distribution and the angular resolution was 2.5 μrad.

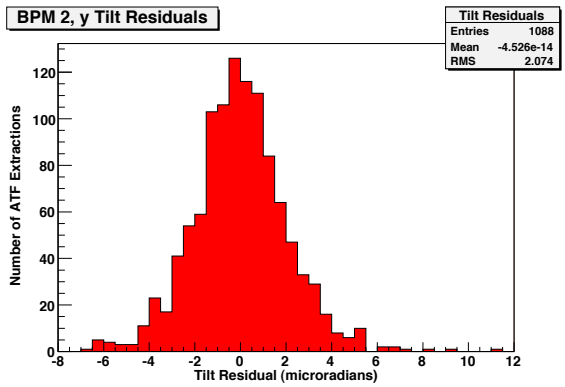

Fig. 28. Tilt residuals for 1088 ATF extractions from 12 April 2006, 2:16 JST. The analysis employed the fitting algorithm with quality cuts and the residuals were calculated from coefficients determined in one regression using the entire data set. The standard deviation of the distribution and the angular resolution was 2.1 μrad.

beam's trajectory as the beam passed through the apparatus, increasing the measured resolution of the BPM system. Assuming that the local static magnetic field was dominated by the earth's magnetic field, and that it was oriented orthogonal to the beam's trajectory (i.e. parallel to the x axis), limits on these effects could be estimated. The earth's

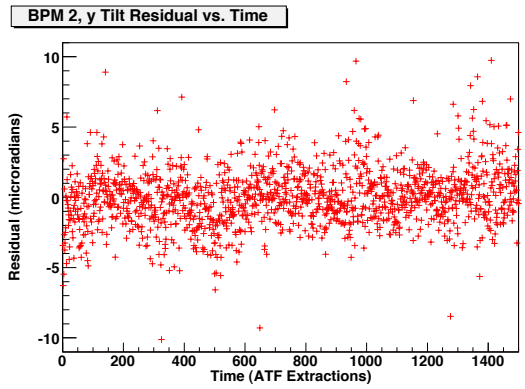

Fig. 29. Tilt residual vs. time for 1454 ATF extractions from 12 April 2006, 2:30 JST. The analysis employed the fitting algorithm with quality cuts and the residuals were calculated from coefficients determined in one regression using the entire data set. The standard deviation of the distribution and the resolution was 2.1 μrad. The lack of structure suggests the resolution was stable over the period the data was taken.

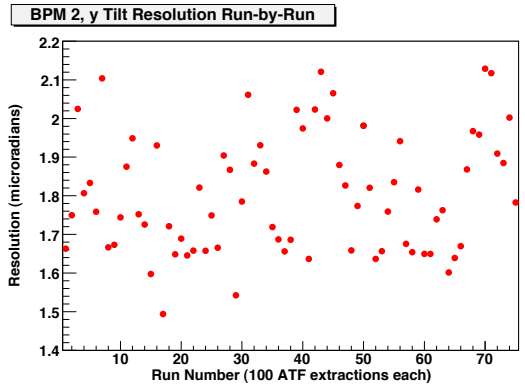

Fig. 30. Tilt resolution for groups of (nominally) 100 sequential bunch crossings from 11 March 2005, 18:38 JST. The analysis employed the fitting algorithm with quality cuts. The mean resolution was 1.4 ± 0.2 μrad.

magnetic field at the ATF on 11 March 2005 was determined to have a total intensity of 46,430.02 nT [16]. The low frequency magnetic fields in the ATF damping ring were measured with a pickup coil, amplifier, and digitizing oscilloscope: The 50 Hz fields were found to be approximately 120 nT, with the integrated field below 50 Hz at approximately 3 nT. Taking $\Delta B = 120$ nT over a given data sample, the effect on the resolution from fluctuations in the local magnetic field was estimated to be 1.3 nm. The stability of the beam energy was investigated by using the measured position of the beam from the 52 BPMs in the ATF arcs. We measured $\Delta E/E = 0.0002$ which was in excellent agreement with the design energy stability of the ATF. The effect on the resolution from this level of energy jitter was estimated to be ≈ 0.07 nm. Both of these effects were well below the computed resolution.

Five temperature sensors were distributed around each BPM assembly with two sensors on the BPM itself, two on the hexapod strut movers, and one on the mounting ring. The data from these sensors were read out on a run-by-run (as opposed to an event-by-event) basis. No correlation was seen between any of the temperature readings and the measured residual.

9. Limits on Resolution

In order to construct a simulated data set free of electronic noise and mechanical vibration, Eq. (48) was used to calculate an ideal beam position in BPM 2, y from the beam parameters measured in the other BPMs (the regression coefficients had to be known for the particular data being used). Starting with an actual data set, for each ATF extraction, the measured position for BPM 2, y was replaced by this ideal beam position. The amplitude and phase of each waveform from BPM 2, y were then computed from this ideal position; amplitudes and phases for all other channels were left unchanged. Decaying sine waves for each channel were then generated from the amplitudes and phases to mimic actual data. If a particular sample value was greater than the ADC maximum (16384 counts) or less than the ADC minimum (0 counts), the sample value was fixed at these limits, thus modeling the saturation seen in actual data. This simulated data was then analyzed as ordinarily using the fitting algorithm.

Amplitude and phase noise could then be added to the generated waveforms. The amplitude noise was determined on a pulse-by-pulse basis from the first 20 samples of the original waveform corresponding to the time prior to the bunch transiting the apparatus. A gaussian distributed random number with a mean of zero and a width equal to the variation in the ADC pedestal value was added to each sample of the generated waveform.

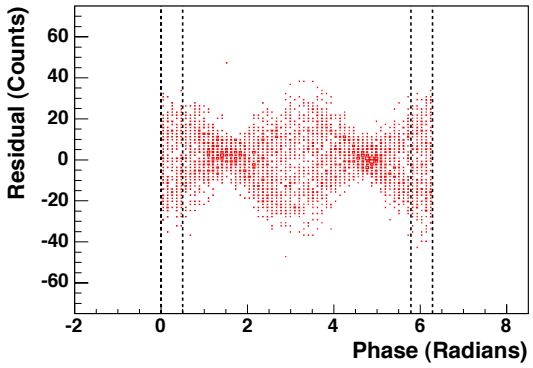

Fig. 31. The "bow-tie" effect: Variation of the residual versus the phase of the test tone. The size of the bow-tie effect was determined from the standard deviation of the fit residuals in the bands indicated from $0 \rightarrow 0.5$ and $2\pi - 0.5 \rightarrow 2\pi$.

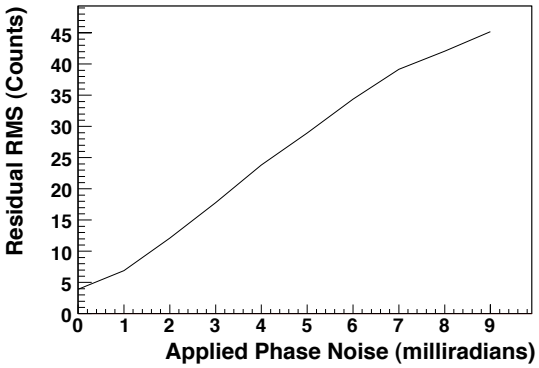

Fig. 32. The correlation between applied phase noise and "bow-tie" size as determined from the standard deviation of the fit residuals. The amplitude noise of ~ 4 ADC Counts attains with zero applied phase noise, as expected.

Determination of the phase noise was rather more involved. Contributions to the phase noise came from both the local oscillators used to down-convert the BPM signals as well as from the digitizer. A tone at the BPM frequency was applied to the electronics and the resultant waveforms, as recorded by the digitizer, were fitted with a sine function

$$V = A\sin(\omega t + \varphi). \tag{69}$$

The contribution to the fit residual from phase noise was found to be proportional to the gradient of the waveform, and resulted in a "bow-tie" effect when plotted against phase $(\omega t + \varphi)$ between 0 and 2π: At points where the slope of the sine wave was large $(\varphi = 0, \pi, 2\pi)$, the residual was also large. A characteristic "bow-tie" plot is shown in Figure 31. Simulated sine waves of the same amplitude as the test-tone data were generated. Thermal noise was applied by adding a gaussian distributed random number to the amplitude, and phase noise was applied by adding a gaussian distributed random number to the phase,

$$V = (A + \sigma_A)\sin(\omega t + \varphi + \sigma_\varphi). \tag{70}$$

Performing the sine wave fit to these waveforms produced the familiar "bow-tie" effect. The size of the "bow-tie" effect was quantified by considering the standard deviation of the residuals from the sine wave fits for phases between $0 \rightarrow 0.5$ and $2\pi - 0.5 \rightarrow 2\pi$. The magnitude of the bow-tie effect was found to be proportional to the amount of phase noise added and disappeared completely if the phase noise was removed altogether, as shown in Fig. 32. The amount of phase noise present in the data could then be estimated from this relation. The estimated phase noise for each channel is shown in Table 7 along with characteristic values for the amplitude noise.

Channel	Characteristic Amplitude Noise (ADC Counts)	Estimated Phase Noise (milliradians)
Reference	4.7	2.3
$1x$	4.1	2.7
$1y$	4.2	2.6
$2x$	4.4	2.5
$2y$	4.0	2.4
$3x$	4.3	2.2
$3y$	4.2	3.1

Table 7
Characteristic amplitude noise and estimated phase noise for each channel.

Table 8 shows the expected resolutions for different scenarios for each of the four data sets. Perhaps most striking, however, were the relatively small contributions from amplitude and phase noise to the overall resolution. Indeed, the contribution to the resolution from other sources was remarkably consistent over the four data sets.

The effect of reducing the attenuation in the reference cavity, and the attendant improvement in its signal-to-noise ratio, became palpable when the resolution with amplitude noise only was compared between the 2005 and 2006 data.

Also particularly noteworthy was the agreement

Run Period	Resolution (nm)					
	Amplitude Noise Only	Phase Noise Only	Amplitude ⊕ Phase Noise	Amplitude and Phase Noise	Best Measured	Contributions from other Sources
11 March 2005, 18:38 JST	9.3	4.2	10.2	10.0	23.8	21.6
27 May 2005, 12:15 JST	13.3	6.2	14.7	14.4	25.4	20.9
12 April 2006, 2:16 JST	2.8	1.3	3.1	2.9	15.6	15.3
12 April 2006, 2:30 JST	2.7	1.7	3.2	3.2	18.6	18.3

Table 8
Limits on resolution from amplitude noise and phase noise. With neither amplitude nor phase noise added back into the simulated waveforms, the resolution is virtually perfect, as expected. Each column in the table details the effect on the resolution of adding the specified type of noise to the waveform samples, performing the analysis with the fitting algorithm, and computing the residuals from coefficients determined in a single regression using the entire data set. Note that adding the resolution with amplitude noise and the resolution with phase noise together in quadrature produces the same result for the resolution as adding both amplitude noise and phase noise to the waveforms. This indicates that amplitude and phase noise are indeed uncorrelated. By subtracting in quadrature the resolution with both amplitude noise and phase noise from the best measured resolution, one may estimate the limit on the resolution from other sources, e.g. non-rigid-body motion of the triplet of BPMs.

between the theoretical expected resolution of 1.8 nm (see Table 4) and the resolution with amplitude noise only (the theoretical expected resolution of 1.8 nm did not take into account phase noise) for the 2006 data of 2.7 nm and 2.8 nm. This is especially true considering that the theoretical expected resolution of 1.8 nm was computed for a bunch containing 1×10^{10} e^- while in practice the ATF bunches typically contained $\sim 0.7 \times 10^{10}$ e^-: Adjusting the 1.8 nm theoretical expected resolution to circumstances yielded 2.6 nm.

10. Conclusions

To date, we have achieved a position resolution of 15.6 nm and a tilt resolution of 2.1 μradians. The position and tilt resolutions were internally consistent with one another. Both the fitting and DDC algorithms generally produced results which were in good agreement.

A consistent picture has emerged suggesting that thermal noise and phase noise in the electronics did not ultimately dominate the measured resolution. There were, however, several additional effects, one or more of which was likely detrimental to the measured resolution at a significant level:

– Machining errors resulting in a coupling slot either offset laterally from or not oriented along the diameter of the cavity would cause coupling of the TM_{010} (monopole) mode to the waveguide: The $\mathcal{Q}_{\rm ext}$ of the TM_{010} mode is roughly proportional to the inverse square of the lateral offset [2]. Given the rather poor measured tolerances of the beam pipe surfaces of the BINP cavities (see Table 2), it was easy to imagine that the TM_{010} mode oscillation, a small portion of which resides at the dipole mode frequency due to the finite $\mathcal{Q}$ of the cavities, may have leaked through imperfect coupling slots and contaminated the dipole mode signals.
– The cavities were, without doubt, elliptic cylinders (as opposed to perfectly round) causing the modes of oscillation to be non-degenerate corresponding to the semi-minor and semi-major axes of the ellipse. If the orientation of the semi-minor and semi-major axes of the ellipse were rotated relative to the x and y axes as defined by the coupling slots, a degree of crosstalk between the x and y modes would naturally have resulted. Signal due to beam offset in x may thus have contaminated the signal due to the beam offset in y, especially considering the relatively large beam instability and corresponding signal voltage in x as compared to y (see Fig. 18). The converse would have been true as well, but to a lesser degree since the beam tended to be much more stable in y.
– Non-rigid-body mechanical motion among the three BPMs may also have contributed to the measured resolution. This mechanical motion could have had any number of origins including acoustic and ground vibrations, and thermal drift.

Our method of considering fluctuations in the ADC pedestal value to determine the amplitude

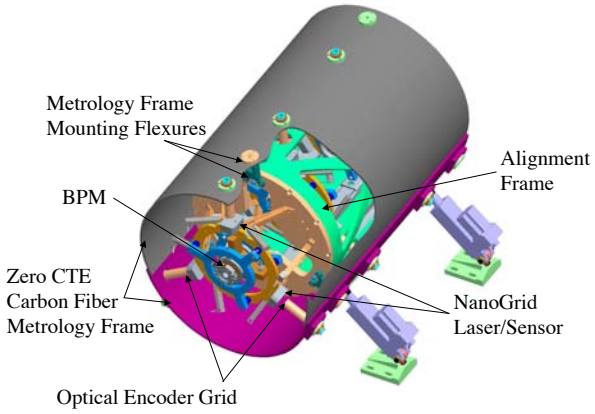

Fig. 33. The recently installed metrology system. Three NanoGrid Model A xy metrology systems are mounted on each BPM to measure its position and orientation relative to optical encoder grids supported by a zero-coefficient of thermal expansion carbon fiber metrology frame surrounding the alignment frame.

noise would have underestimated in the presence of either monopole mode contamination or crosstalk. These two effects have proven difficult to quantify empirically. Precise measurements of the cavity surfaces with a CMM would shed considerable light on these effects, but because such measurements would require the destruction of the cavities, they have not been performed as of this writing.

A metrology system for the three BPMs has recently been installed. Mounted on each BPM are three NanoGrid Model A Hi-Resolution systems manufactured by Optra Inc. [17]. The Optra NanoGrid is an xy metrology system that measures the position of a combination laser/sensor relative to an optical encoder grid. A zero-coefficient of thermal expansion (CTE) carbon fiber metrology frame supports the optical encoder grids. Each laser/sensor of the NanoGrid A Hi-Resolution system is capable of measuring planar displacements with a resolution of 0.3 nanometers relative to its encoder grid. By using three NanoGrid systems per BPM, the overall position and orientation in space of each BPM can be precisely determined relative to the carbon fiber metrology frame. The metrology system is illustrated in Fig. 33. This system should make possible an evaluation of the non-rigid-body mechanical motion among the three BPMs and in particular that part due to thermal drifts. Tests with the new metrology system are in progress as of this writing.

11. Acknowledgments

We wish to thank the operators and support staff at the ATF for all of their kind help and invaluable expertise during these experiments.

References

[1] Draft letter of intent for the LINX test facility at SLAC. http://www-project.slac.stanford.edu/lc/linx /papers/LINX_07-15-01.pdf.

[2] Z. Li, R. Johnson, S. R. Smith, T. Naito, and J. Rifkin. Cavity BPM with dipole-mode selective coupler. In *Proceedings of the 2003 Particle Accelerator Conference*, Portland, OR, 2003. IEEE.

[3] J. D. Jackson. *Classical Electrodynamics, Second Edition.* John Wiley and Sons, New York, 1975.

[4] M. Abramowitz and I. A. Stegun. *Handbook of Mathematical Functions.* Dover Publications, Inc., New York, 1965.

[5] Alexey Lyapin. *Strahllagemonitor fuer das TESLA-Energiespektrometer.* Dissertation, TU-Berlin, Berlin, 2003.

[6] D. H. Whittum and Y. G. Kolomensky. Analysis of an asymmetric resonant cavity as a beam monitor. *Reviews of Scientific Instruments*, 70:2300, 1999.

[7] V. Balakin et al. Discussion of nanobeam summaries and areas for future collaboration. http://www.vlepp.serpukhov.su/engl/bnl/bpm.html.

[8] N. Solyak. Private communication.

[9] C. P. Reeve. *The Calibration of a Roundness Standard.* NBSIR 79-1758, 1979.

[10] David J. Jackson, Dong Su, and Fred J. Wickens. Internal alignment of the SLD vertex detector using a matrix singular value decomposition technique. *Nucl. Instrum. Meth.*, A491:351–365, 2002.

[11] The GdfidL electromagnetic field simulator. http://www.gdfidl.de.

[12] Devendra K. Misra. *Radio-Frequency and Microwave Communication Circuits, Second Edition.* John Wiley and Sons, New York, 2004.

[13] ROOT data analysis framework. http://root.cern.ch/.

[14] MINUIT physics analysis tool for function minimization.

http://seal.web.cern.ch/seal/snapshot/work-packages/mathlibs/minuit/.

[15] MATLAB language and interactive environment. http://www.mathworks.com/.

[16] The latitude and longitude of the ATF were determined with a handheld GPS receiver. The earth's magnetic field and the rate of change of the field for that location for the date 11 March 2005 were then found on the website of the National Geophysical Data Center (NGDC) of the NOAA Satellite and Information Service: http://www.ngdc.noaa.gov/seg/geomag/jsp/struts/calcPointIGRF.

[17] Optra Inc. http://www.optra.com/.